Platelet concentrate-derived extracellular vesicles promote adult hippocampal neurogenesis

Ariunjargal NyamErdene[1], Nhi Thao Ngoc Le[1], Ouada Nebie[2], Emilie Faivre[2,3], Liling Delila [4], Ming-Li Chou[4], Joshua R Lowe[5], Kadiombo Bantubungi[6], Luc Buée[2,3], Tara L Walker[5], David Blum[2,3,4*], Thierry Burnouf[1,4, 7,8*]

[1] International Ph.D. Program in Biomedical Engineering, College of Biomedical Engineering, Taipei Medical University, Taipei, Taiwan
[2] University of Lille, Inserm, CHU Lille, UMR-S1172 Lille Neuroscience & Cognition (LilNCog), Lille, France
[3] Alzheimer and Tauopathies, LabEx DISTALZ, France
[4] Graduate Institute of Biomedical Materials and Tissue Engineering, Taipei Medical University , Taipei, Taiwan
[5] Clem Jones Centre for Ageing Dementia Research, Queensland Brain Institute, The University of Queensland, Brisbane, Australia
[6] Inserm UMR-1011, University of Lille, Lille, France
[7]International Ph.D. Program in Cell Therapy and Regeneration Medicine
[8]Ph.D. Program in Graduate Institute of Mind Brain and Consciousness, College of Humanities and Social Sciences, Taipei Medical University, Taipei, Taiwan

*Correspondence:
Thierry Burnouf, Graduate Institute of Biomedical Materials and Tissue Engineering, College of Biomedical Engineering, Taipei Medical University Shuang-Ho campus, No. 301, Yuantong Rd., Zhonghe Dist., New Taipei City 235, Taiwan. Email: thierry@tmu.edu.tw; thburnouf@gmail.com
David Blum, University of Lille, Inserm, CHU Lille, UMR-S1172 Lille Neuroscience & Cognition (LilNCog), Lille, France. Email: david.blum@inserm.fr

ORCID profile: AN, 0000-0002-2901-0486; NTNL, 0000-0002-9540-8564; ON, 0000-0002-6802-4215; EF, 0000-0002-8608-9848; LD, 0000-0003-4979-3489; MC, 0000-0002-6996-5332; KB, 0000-0002-6152-5623; LB, 0000-0002-6261-4230; TW, 0000-0002-8472-0245; DB, 0000-0001-5691-431X; TB, 0000-0002-0507-9243

ABSTRACT

Platelet-derived materials are emerging as promising, cell-free biotherapies for regenerative medicine. While platelet lysates have shown neuroprotective activity in preclinical models, the neurogenic potential of platelet concentrate-derived extracellular vesicles (pEVs) remains underexplored. Here, we evaluated the effects of human pEVs and a neuroprotective heat-treated human platelet lysate (HPPL) on adult hippocampal neurogenesis using both an ex vivo neurosphere assay and an in vivo intranasal administration model. pEVs selectively enhanced dentate gyrus (DG)-derived neurosphere growth, even in the absence of exogenous growth factors, and were internalized by neural precursors. In vivo, short-term pEV delivery increased EdU^+ proliferating cells in the DG, while long-term administration (28 days) elevated the proportion of newborn mature neurons. By contrast, HPPL primarily promoted early neurogenesis by expanding immature DCX^+ neurons. Quantitative proteomics of DG tissue after pEV treatment revealed 111 differentially expressed proteins, with enrichment in pathways related to oxidative phosphorylation, Notch4 signaling, myelination, and MHC class I-mediated antigen presentation. Downregulated proteins included cytoskeletal and translation-related regulators, suggesting a shift toward neuronal differentiation and circuit integration. Biophysical characterization confirmed the purity and vesicular nature of pEVs, with a defined protein cargo including immune modulators and ECM-interacting molecules such as CD44, lymphatic vessel endothelial hyaluronan receptor 1 (LYVE1), and complement proteins. These findings identify allogeneic pEVs as multifunctional agents that modulate neural precursor cell fate and brain tissue remodeling through coordinated metabolic and immunoregulatory mechanisms. This work supports the translational potential of pEV-based therapeutics for promoting hippocampal neurogenesis and cognitive repair in neurodegenerative and age-related brain disorders.

Keywords: Platelet extracellular vesicles, platelet lysates, neurogenesis, regenerative medicine, intranasal delivery, brain repair.

67 # 1. Introduction

68

69 Adult neurogenesis, the process by which neural stem/progenitor cells (NSPCs) generate new
70 neurons and contribute to brain plasticity [1], continues throughout life in discrete brain regions,
71 notably the subventricular zone (SVZ) and the subgranular zone (SGZ) of the hippocampal dentate
72 gyrus (DG) [2, 3]. This process plays an essential role in cognition, memory formation, affective
73 functions, and mood regulation [4, 5]. However, neurogenesis progressively declines with aging
74 and is impaired in neurodegenerative and neuropsychiatric disorders such as Alzheimer's disease
75 and major depressive disorder [6, 7]. While physical activity [8, 9], environmental enrichment
76 [10], and systemic trophic factors [11] can partially counteract this decline, there is a growing need
77 for targeted, minimally invasive therapies to restore neurogenic capacity and neural circuit
78 function [12].

79 Platelet-derived biomaterials are emerging as promising candidates for regenerative medicine
80 owing to their inherent multifaceted bioactivity, abundance, and favorable safety profile [13].
81 Platelet concentrates (PCs), used routinely for transfusion, are a clinically available and scalable
82 source of lysates and extracellular vesicles (EVs) that contain a rich array of growth factors,
83 cytokines, antioxidants and anti-inflammatory factors [13]. Upon activation, platelets release
84 extracellular vesicles (pEVs), nanoscale particles (50–200 nm) with a phospholipid bilayer that
85 protects and transports cargo including proteins, nucleic acids, and metabolites [14]. These vesicles
86 share some functional similarities and therapeutic potentials with mesenchymal stromal cell-
87 derived EVs [15] and can be produced consistently under GMP-compliant conditions thanks to
88 pooling strategies [13]. Several trophic factors abundant in platelet lysates and pEVs, such as
89 brain-derived neurotrophic factor (BDNF), platelet-derived growth factor (PDGF), vascular
90 endothelium growth factor (VEGF), epithelium growth factor (EGF), and platelet factor 4 (PF4;
91 CXCL4) [16, 17] are individually known to exert neuroprotective effects in models of stroke [18],
92 traumatic brain injury [19, 20] and neurodegeneration [21-24]. PF4, in particular, has recently been
93 identified as a circulating exerkine that promotes hippocampal neurogenesis and improves
94 cognitive function in aging models [9, 11]. These findings provide a strong biological rationale for
95 investigating platelet-derived products as naturally enriched, multimodal agents for brain repair
96 and neurorestoration [25-27]. pEVs can cross biological barriers and be taken up by recipient cells
97 via endocytosis or membrane fusion, making them attractive for regenerative applications [13, 28].

98 Their capacity to modulate inflammation, angiogenesis, and oxidative stress has been
99 demonstrated in cardiovascular [29], corneal injury models [30, 31] and wound healing [32]. Yet,
100 the potential of native PC-derived EVs capable of stimulating adult hippocampal neurogenesis
101 remains unexplored.

102 In this study, we systematically assessed the neurogenic effects of two platelet-derived
103 products, heat-treated human platelet pellet lysate (HPPL) [19, 21] and PC-derived EVs on neural
104 precursor cells in the DG. Using ex vivo neurosphere assays and in vivo intranasal delivery in
105 adult mice, we evaluated their ability to stimulate NSPC proliferation, differentiation, and
106 maturation. In parallel, we performed proteomic profiling of hippocampal tissue to elucidate the
107 molecular pathways modulated by these treatments. By leveraging the natural regenerative cargo
108 of platelet-derived vesicles and lysates, this work identifies novel, biocompatible biomaterials with
109 potential for treating aging-related cognitive decline and neurodegenerative diseases through the
110 enhancement of endogenous neurogenesis.
111

112 ## 2. Material and Methods

113 *2.1. Preparation and characterization of platelet materials*
114

115 *2.1.1. Serum-converted platelet lysate (SCPL) and human platelet pellet lysate (HPPL)*
116

117 Therapeutic-grade human PCs were collected from healthy volunteers at the Taipei Blood Center
118 under Institutional Review Board approval (TMU-JIRB N201802052). These allogeneic PCs were
119 suspended in 100% plasma, anticoagulated with citrate-phosphate dextrose solution A, and
120 collected using the MCS+ system (Haemonetics, USA) and transported within 90 minutes under
121 controlled temperatures to Taipei Medical University (TMU). PCs were stored on a slow-speed
122 agitator at 22 ± 2 °C until processing within 24 hours. For this study, at least three PC units were
123 initially pooled to generate both heat-treated platelet pellet lysate (HPPL) and serum-converted
124 platelet lysate (SCPL), which was subsequently used for extracellular vesicle (EV) isolation and
125 functional assays. All preparations were performed under aseptic conditions. To prepare SCPL,
126 0.3 mL of 0.9 M $CaCl_2$ and 5 g of sterile glass beads were added to every 10 mL of PC to induce
127 coagulation and platelet activation. The mixture was rotated at room temperature until clot
128 formation, followed by an additional 30-minutes rotation. Samples were centrifuged at 6,000 × g

129 for 30 minutes, and the supernatant (SCPL) was collected, aliquoted, and stored at −80 °C until
130 EV isolation.[33] To prepare HPPL, PCs were centrifuged at 3,000 × g for 30 minutes at 22 °C to
131 pellet platelets. Plasma was removed, and platelet pellets were washed with PBS and concentrated
132 to one-tenth of their original volume. The concentrated platelets underwent three freeze-thaw
133 cycles (−80 ± 1 °C to 37 ± 1 °C), followed by centrifugation at 4,500 × g for 30 minutes at 20 ± 1 °C.
134 The lysate was then heat-treated at 56 ± 1 °C for 30 minutes, cooled on ice for at least 5 minutes,
135 and centrifuged at 10^4 × g for 15 minutes at 4 ± 2 °C to remove precipitates.[21] For all experiments,
136 HPPL was aliquoted (100 µL) in 1.5 mL Eppendorf tubes and stored at −80 °C until use.
137
138 *2.1.2. Isolation of platelet extracellular vesicles (pEVs)*
139
140 Platelet concentrate-derived EVs (pEVs) were isolated and characterized as previously described
141 [33]. Briefly, pEVs were purified from SCPL using size exclusion chromatography (SEC). A
142 Merck Vantage L Laboratory column (VL 11 × 250 mm), packed with 10 mL of Sepharose CL-
143 2B (Sigma-Aldrich, GE Healthcare Bio-Sciences, Sweden), was used for SEC with a flow rate of
144 1.2 mL/min. A 0.5 mL aliquot of SCPL was injected per run and eluted using PBS containing
145 0.32% sodium citrate (pH 7.4) as the running buffer [34]. pEV-enriched fractions were collected
146 and pooled. Pooled fractions were concentrated using Amicon Ultra-4 centrifugal filter devices
147 (50K cutoff, Merck Millipore) by centrifugation at 4,000 × g for 25 minutes. For experimental use,
148 pEVs were aliquoted (100 µL) into 1.5 mL Eppendorf tubes and stored at −80 °C until use in ex
149 vivo and in vivo assays.
150
151 *2.1.3. Biochemical and biophysical characterization of platelet materials*
152
153 Total protein content in pEVs and HPPL was measured using a bicinchoninic acid (BCA) assay
154 (Thermo Scientific, Cat# 23227). Particle concentration and size distribution were analyzed by
155 nanoparticle tracking analysis (NTA) using a NanoSight NS300 system (Malvern), with samples
156 diluted in 0.22 µm-filtered PBS to achieve 50–200 particles per frame. Each sample underwent
157 five 60-second recordings, analyzed using NTA software (v3.4). In addition, dynamic light
158 scattering (DLS) was used to assess size distribution using a Zetasizer Lab instrument (Malvern)
159 and Zetasizer software (v7.13).

160

161 *2.1.4. Cryo-electron microscopy (cryo-EM) of SCPL and pEVs*

162

163 Crude SCPL and SEC-purified EV samples were prepared for cryo-electron microscopy (cryo-
164 EM) to assess vesicle morphology. A 4 µL aliquot of either SCPL-raw (obtained by serum
165 conversion of platelet concentrates) or SEC-purified SCPL-EVs (resuspended in PBS-citrate used
166 to equilibrate the SEC column) was applied to separate 200-mesh holey carbon grids. Grids were
167 glow-discharged for 20 seconds using a plasma cleaner (Electron Microscopy Sciences) to
168 improve surface hydrophilicity. Samples were blotted for 3 seconds under 100% humidity at 4 °C
169 and immediately vitrified using a FEI Vitrobot Mark II. Grids were stored in liquid nitrogen until
170 imaging. Micrographs were acquired at optimal magnification using a FEI Tecnai F20
171 transmission electron microscope, operated by staff at the Cryo-EM Core Facility, Academia
172 Sinica, Taipei, Taiwan.

173

174 *2.1.5. Electrophoretic protein profiling of pEVs and HPPL*

175

176 To visualize the protein composition of EVs and HPPL, sodium dodecyl sulfate–polyacrylamide
177 gel electrophoresis (SDS-PAGE) was performed. A total of 20 µg of protein from each sample
178 was mixed with XT sample buffer (Bio-Rad, Cat# 1610791) and heated at 95 °C for 5 minutes,
179 either in the presence or absence of reducing agent (Invitrogen, Cat# NP0009). Samples were then
180 loaded onto a precast NuPAGE 4–12% Bis-Tris protein gel (1.0 mm; Invitrogen, Cat#
181 NP0321BOX). For reduced samples, antioxidant (Invitrogen, Cat# NP0005) was added to the
182 running buffer according to the manufacturer's protocol. Electrophoresis was initially run at 60 V
183 for 30 minutes, followed by 125 V for the remainder of the run (Power supply: T-Pro
184 Biotechnology, Model JB07-G003). After separation, gels were stained with InstantBlue
185 Coomassie protein stain (Abcam, Cat# ab119211) for 15 minutes. Protein bands were visualized
186 using a white-light transilluminator and documented with a digital camera.

187

188 *2.1.6. Detection of pEVs surface markers in EVs*

189

190 A human-specific antibody membrane array (EXO-RAY210B-8, System Biosciences) was used
191 to detect EV surface markers following the manufacturer's instructions. EVs (50 µg total protein)
192 were lysed in the provided buffer, and 1 µL of labeling reagent was added. Samples were incubated
193 with continuous mixing for 30 minutes at room temperature. Excess labeling reagent was removed
194 using the included separation column and wash steps. The labeled lysate was mixed with 5 mL of
195 blocking buffer and applied to the antibody array membrane, followed by overnight incubation at
196 4 °C on a shaker. After washing, membranes were incubated with detection reagents for 30 minutes
197 at room temperature. Streptavidin-HRP (5 µg/mL) and chemiluminescent substrates were then
198 applied. Signal detection was performed using the UVP BioSpectrum 810 imaging system. Band
199 intensities were quantified by subtracting background values from each target signal using the
200 array software.
201
202 *2.1.7. Quantification of pEVs and platelet markers in EVs by nano flow cytometry (nFCM)*
203
204 Surface marker expression of EV-specific and platelet-derived antigens in pEVs was analyzed
205 using nano flow cytometry (nFCM). Samples were stained with fluorescently conjugated
206 antibodies against CD9, and CD41followed by incubation at 37 °C. After staining, samples were
207 washed with PBS and ultracentrifuged at 100,000 × g for 70 minutes at 4 °C. Pellets were
208 resuspended in PBS for subsequent analysis. To ensure optimal detection, samples were diluted to
209 achieve particle acquisition rates between 2,000 and 12,000 events per minute. Particle size
210 distribution, concentration, and surface marker expression were assessed using a NanoFCM flow
211 cytometer. Data were processed with NanoFCM Profession software (version 2.330), with vesicle
212 size and concentration calculated from flow rate and side scatter intensity, using standard
213 calibration curves.
214
215 *2.2. Ex vivo neurosphere assay*
216
217 *2.2.1. Animals*
218 Eight-week-old adult female C57BL/6J mice (n = 15) were obtained from the Taiwan National
219 Laboratory Animal Center (Nangang, Taipei, Taiwan) and used for neural precursor cell isolation.

220 All procedures were conducted in accordance with institutional ethical guidelines and approved
221 by the Institutional Animal Care and Use Committee of TMU (Protocol No. SHLAC2023-0050)
222
223 *2.2.2 Neural precursor cell culture*
224
225 Neural precursor cells were isolated from the dentate gyrus (DG) of the hippocampus of 8-week-
226 old female C57BL/6J mice, as previously described [35]. DG tissues were dissected and processed
227 separately. DG tissue was minced and enzymatically digested at 37 °C for 14 minutes: DG samples
228 with papain, with intermittent gentle agitation. Following digestion, DG cells were dissociated
229 mechanically by gentle pipetting. Cell suspensions were incubated for an additional 10 minutes,
230 centrifuged at 300 × g for 5 minutes, and resuspended in hank's balanced salt solution (HBSS).
231 The suspensions were passed through a 40 µm cell strainer (Corning, Cat No. 431750) to remove
232 debris. After final centrifugation, cell pellets were resuspended in 200 µL of complete growth
233 medium composed of Neurobasal medium [Gibco #21103-049], with 2% B-27 [Gibco #17504-
234 044], 1% penicillin/streptomycin (10,000 U/mL), [Gibco #15140122], 1% GlutaMAX [Fisher
235 Scientific #35050061], and 20 ng/mL each of EGF [Sigma #AF-100-15] and FGF-2 [Sigma #100-
236 18B]). In some experiments, EGF and FGF-2 were not included and replaced by pEVs or HPPL.
237 For proliferation assays, cells were cultured with 0.5% pEVs, 0.5% HPPL, or no supplementation
238 (control). Neurosphere formation was assessed after 10 days.
239
240 *2.2.3. Proliferation assay*
241
242 The proliferation assay was performed as previously described [35]. Briefly, neural precursor cells
243 from DG were cultured in proliferation medium supplemented with either 0.5% pEVs or 0.5%
244 HPPL. Control wells received no supplementation. After 10 days of culture, proliferation was
245 assessed by counting the number of neurospheres in 80 wells of a 96-well plate per condition and
246 measuring their diameter of 50 randomly selected neurospheres using a light microscope (Leica).
247 Additionally, to evaluate the proliferative effects of platelet-derived materials in the absence of
248 exogenous mitogens, a separate set of three independent experiments was performed using
249 medium lacking EGF and FGF-2. In these assays, 0.5% pEVs or HPPL was added as the sole
250 supplement, and unsupplemented medium served as a negative control. All measurements were

251 performed in a blinded manner to avoid bias, with experiments repeated independently five times
252 (n = 5).
253
254 *2.2.4. Alexa fluor 488 Labeling of pEVs and HPPL and their internalization in neurospheres*
255
256 pEVs and HPPL were covalently labeled with Alexa Fluor 488 using the Protein Labeling Kit
257 (A10238, Thermo Fisher Scientific) per manufacturer's instructions. Samples were resuspended in
258 0.1 M sodium bicarbonate buffer (pH 8.3) at 1 mg/mL, combined with reconstituted Alexa Fluor
259 488 dye in a 1:10 protein ratio, and incubated overnight at 4 °C in darkness with gentle agitation.
260 Labeled products were purified using the provided columns pre-equilibrated with elution buffer,
261 washed with PBS to remove unbound dye, and stored at 4 °C for up to two weeks. Labeling
262 efficiency was confirmed by measuring absorbance/emission at 555/565 nm. For internalization,
263 neurospheres from DG (10-day culture) were grown in low-adhesion plates with supplemented
264 neurobasal medium, then incubated with labeled pEVs and HPPL (10-50 µg/mL) for 24 hours at
265 37 °C with 5% CO_2. After PBS washing, neurospheres were transferred to coated coverslips, fixed
266 with 20% cold methanol, stained with DAPI (1:5000), and imaged using Stellaris microscope with
267 Z-stack to visualize 3D internalization within the neurospheres.
268
269 *2.3. In vivo neurogenesis*
270
271 The primary animal study was conducted at the ULille Animal Research Center (Inserm), and a
272 replication animal study was performed at the Taipei Medical University (TMU) Shuangho animal
273 facility. Mice at both facilities were housed under standard conditions (12-hour light/dark cycle;
274 temperature 18.5–24 °C; humidity 40–60%). Animals were allowed to acclimate for one week
275 prior to the start of experiments. All procedures were conducted in accordance with institutional
276 ethical guidelines and approved by the Institutional Animal Care and Use Committee of ULille
277 and TMU (APAFIS 43474-2023050714441306 and SHLAC2023-0050).
278
279 *2.3.1. Intranasal (i.n) administration of pEVs and HPPL for short-term neuronal proliferation and*
280 *long-term maturation analysis*
281

282 pEVs, HPPL, and PBS vehicle (control) were prepared in 100 µL aliquots and thawed immediately
283 prior to use. A total volume of 30 µL was administered intranasally (i.n.) to 8-week-old female
284 C57BL/6J mice (n = 18 per group) while mice were held in an upright position. The administration
285 followed a precise protocol where small drops (2-3 µL each) were delivered alternately to each
286 nostril with 1-2 minutes intervals between drops until the total dose of 30 µL was reached. For
287 short-term proliferation analysis, mice received daily intranasal administration for three
288 consecutive days (total of 3 doses). For long-term neurogenesis assessment, a separate cohort
289 received intranasal administration every 3rd day until D27 and sacrificed at D28 days (total of 11
290 doses).
291
292 *2.3.2. 5-Ethynyl-2′-Deoxyuridine (EDU) injection*
293
294 To label proliferating neural precursor cells for both short-term and long-term neurogenesis
295 assesments, mice received six intraperitoneal (i.p.) injections of 5-ethynyl-2′-deoxyuridine (EdU;
296 50 mg/kg; Sigma, 900584), a thymidine analog that incorporates into DNA during the S-phase of
297 the cell cycle [36]. Injections were administered twice daily (T0 and T6 hours) for three
298 consecutive days starting 2 hours after the first i.n. administration of pEVs, HPPL, or PBS vehicle.
299 EdU was freshly prepared in sterile, filtered PBS and dissolved immediately prior to injection.
300 Body weights were monitored at baseline (week 0), week 2, and week 4 to assess general health
301 during the study period.
302
303 *2.3.3. Histological procedures*
304
305 Mice were deeply anesthetized using a combination of Zoletil 50 (50 mg/mL; Sigma) and Xylazine
306 (23.32 mg/mL; Sigma), diluted in double-distilled water. Transcardial perfusion was performed
307 with cold 0.9% NaCl, followed by 4% paraformaldehyde (PFA) in 0.1 M phosphate buffer (pH 7.4).
308 Brains were dissected and post-fixed in 4% PFA for 24 hours at 4 °C, then cryoprotected in 30%
309 sucrose (JT Baker) for 48 hours. Following cryoprotection, brains were immersed in pre-cooled
310 isopentane (–35 to –40 °C) for 1 minute and stored at –80 °C until sectioning. Coronal sections
311 (35 µm) were collected for proliferation analysis, and sagittal sections (35 µm) from one
312 hemisphere were used for neuronal maturation studies. Sections were obtained using a Leica

313 CM3050S cryostat (TMU core facility), transported on dry ice, and stored in PBS containing 0.2%
314 (w/v) sodium azide at 4 °C until use.
315
316 *2.3.4. Immunofluorescence protocol*

317 Free-floating brain sections spaced 350 µm apart, spanning the dorsal dentate gyrus to the lateral
318 ventricles (Bregma –1.34 to –2.70 mm), were collected in ten series per animal. Sections were
319 washed in cold PBS and permeabilized in PBS containing 0.2–0.5% Triton X-100 for 30 minutes
320 with gentle agitation. For EdU staining, slices were blocked in 3% BSA in PBS for 20 minutes,
321 followed by a second permeabilization with 0.5% Triton X-100 for 20 minutes. After an additional
322 20-minutes blocking step, sections were incubated with the EdU Click-iT cocktail (Thermo Fisher)
323 for 30 minutes at room temperature. Sections were then rinsed three times in PBS with 3% BSA
324 and counterstained with DAPI (1:500; Thermo Fisher, 62248) for 5 minutes. For co-staining with
325 neuronal markers, slices were incubated in a mouse-on-mouse blocking reagent (Vector MKB2213,
326 1:100 in 0.2% Triton X-100 PBS) for 1 hour. Primary antibody staining was performed with mouse
327 anti-NeuN-biotinylated (Millipore MAB377B; 1:500 in 1% normal goat serum) and anti-DCX
328 (1/250, Millipore Ab2253, LOT2881137) for 48 hours at 4 °C. Following PBS washes, sections
329 were incubated with Streptavidin-Alexa Fluor 568 (Invitrogen S11226; 1:500) for 1–2 hours at
330 room temperature. After staining, sections were mounted on adhesive slides and air-dried in the
331 dark. Autofluorescence was quenched by sequential treatment with 70% ethanol (5 minutes), 0.1%
332 Sudan Black B in 70% ethanol (5 minutes), and a final 70% ethanol rinse (1 minute). Slides were
333 washed in 0.9% NaCl and coverslipped using DAKO fluorescent mounting medium (DAKO
334 S3023).

335
336 *2.3.5. Image acquisition*
337
338 Brain tissues from C57BL/6J mice (n = 18 per group) were processed for immunofluorescence
339 and stained with EdU and/or NeuN. Brain sections were scanned using the TissueFAXS slide
340 scanning system (ZEISS, model 1025727155) at 20× magnification (120 slides total), and
341 representative images were captured using Stellaris confocal microscopy with 63× objectives.
342 Each animal contributed 3–5 comparable coronal brain sections for analysis. Quantification of

343 positively stained cells was performed using HistoQuest software (TissueGnostics, version 5).
344 Fluorescence intensities were analyzed across individual channels, and events were recorded as
345 counts per region. Analyses were focused on the hippocampal DG, corresponding to Bregma
346 coordinates –1.34 to –2.70 mm, based on the Allen Brain Atlas.
347
348 *2.3.6. Sample processing for proteomics*

349 For pEV and HPPL samples, protein precipitation was performed using cold acetone. Acetone was
350 pre-cooled to −20°C for at least 24 hours prior to sample preparation. The pEV and HPPL samples
351 were mixed with cold acetone at a 1:4 ratio. After vortexing, the samples were incubated overnight
352 at −20°C. The next day, samples were centrifuged at 15,000 × g for 10 minutes at 4°C. The
353 supernatant was discarded, and the pellets were washed twice with cold acetone/water (4:1),
354 followed by centrifugation at 15,000 × g for 10 minutes after each wash. Pellets were air-dried on
355 ice and then resuspended in 6 M urea (prepared by dissolving 1.8 g of urea in 5 mL of water).
356 Protein concentrations were measured using the BCA assay, and the final concentration was
357 adjusted to at least 1 μg/μL. Approximately 100 μg of protein was submitted to the National
358 Taiwan University (NTU) Proteomics Core Facility for LC-MS/MS analysis. In-solution digestion
359 was performed at NTU. Briefly, proteins were reduced with 5 mM DTT at 29°C for 45 minutes,
360 then alkylated with 10 mM iodoacetamide in the dark at 29°C for another 45 minutes. Trypsin was
361 added at a 1:50 (enzyme, w/w) ratio for overnight digestion (16 h) at 29°C. Digestion was stopped
362 by adding 10% TFA to a final concentration of 0.5%. Samples were desalted using C18 columns
363 prior to LC-MS/MS analysis

364 *2.3.7. Mouse tissues of dentate gyrus (DG) following pEVs and PBS treatment*

365 DG tissues were collected at 28 days post-intranasal administration (dpi) from mice treated with
366 PBS (n = 3) and pEVs (n = 3). Proteins were homogenized using ice-cold 10 mM Tris base (pH
367 7.4) containing 10% sucrose (0.32 M). Samples were sonicated on ice at 10% amplitude (10 sec
368 on/5 seconds off, total 1 minute), maintaining temperature below 30°C. Lysates were homogenized
369 for 1 hour at 4°C using a rotor. After centrifugation at 15,000 × g for 10 minutes, supernatants
370 were collected, and protein concentration was immediately determined by BCA analysis.

371 For LC-MS/MS, 200 µg of total protein was precipitated with cold acetone (1:4, v/v) and incubated
372 overnight at –20°C. Samples were centrifuged (15,000 × g, 10 min, 4°C), washed twice with cold
373 acetone, air-dried, and resuspended in 6 M urea. Following re-quantification, tissues from 3 mice
374 per group were pooled to obtain 100 µg of protein per sample. In-solution digestion was performed
375 at NTU, where proteins were reduced with 5 mM DTT at 29°C for 45 minutes, then alkylated with
376 10 mM iodoacetamide in the dark at 29°C for another 45 minutes. Trypsin was added at a 1:50
377 (enzyme, w/w) ratio for overnight digestion (16 h) at 29°C. Digestion was stopped by adding 10%
378 TFA to a final concentration of 0.5%. Samples were desalted using C18 columns prior to LC-
379 MS/MS analysis. Fresh samples were submitted to the National Taiwan University (NTU)
380 Proteomics Core Facility for LC-MS/MS using an Orbitrap Fusion Lumos Tribrid quadrupole-ion
381 trap-Orbitrap mass spectrometer (Thermo Fisher Scientific).

382 *2.3.8. Bioinformatic analysis of proteomics data*

383 Raw data were analyzed using the Mascot search engine integrated in Proteome Discoverer
384 software (version 2.2, Thermo Scientific). Searches were conducted against the most recent
385 UniProt (Swiss-Prot) mouse protein database (release: 2023), with parameters including: trypsin
386 as the digestion enzyme, maximum of two missed cleavages, precursor mass tolerance of 10 ppm,
387 and fragment mass tolerance of 0.02 Da. Carbamidomethylation of cysteine was set as a fixed
388 modification, while oxidation of methionine and N-terminal acetylation were set as variable
389 modifications. Peptide-spectrum matches were filtered at both protein and peptide levels using a
390 target-decoy strategy. For protein identification, high-confidence peptide-spectrum matches
391 (PSMs) were filtered using a false discovery rate (FDR) of 1%, with additional filters including
392 "IsMasterProtein" and Mascot score ≥ 30. Only proteins quantified in both technical replicates
393 were included in the analysis. Differentially expressed proteins (DEPs) were identified using a
394 two-tailed unpaired t-test assuming unequal variances (heteroscedastic). Proteins with a fold-
395 change ≥ 1.2 or ≤ 0.83 and a p-value < 0.05 were considered significantly differentially expressed.
396 Gene Ontology (GO) enrichment analysis was conducted using DAVID Bioinformatics Resources
397 6.8, while canonical pathways and upstream regulators were further analyzed with Ingenuity
398 Pathway Analysis (IPA, Qiagen).

399 *2.4. Statistical analysis*

All data are presented as mean ± standard deviation (SD) or standard error of the mean (SEM), as indicated in figure legends. Statistical analyses were performed using GraphPad Prism (version 10.2.3; GraphPad Software, La Jolla, CA, USA). Differences among the pEVs, HPPL, and control groups were assessed using ordinary one-way ANOVA followed by Dunnett's multiple comparisons test to compare treatment groups against the control. A p value < 0.05 was considered statistically significant. The number of independent biological replicates for each experiment is indicated in the corresponding figure legends.

3. Results

3.1. Characterization of platelet-derived extracellular vesicles (pEV): comparative analysis with heat-treated pellet platelet lysates (HPPL) for neurogenesis application

We isolated extracellular vesicles (EVs) from serum-converted platelet lysates using size exclusion chromatography with Sepharose CL-2B resin, following established protocols [37]. Both pEVs and HPPL were generated from pooled platelet concentrates (n=3) obtained from Taipei Blood Center (Fig. 1A). To confirm the specific characteristics of pEVs, we first characterized the samples based on their morphology. Cryo-electron microscopy confirmed the presence of membrane-bound vesicles in pEVs preparations, displaying typical cup-shaped morphology with sizes around 100 nm (Fig. 1B). For comparison, cryo-EM images of the raw materials (serum-converted platelet lysates) shown in (Fig. 1B-left) revealed an unclear lipid layer with a dirty background surrounded by other lipids, in contrast to the isolated EVs with their distinct membrane structures.

The morphological observations were further validated by size distribution analysis. Dynamic light scattering revealed that pEVs exhibited a uniform size distribution with a mean diameter of 164.8 nm (Fig. 1C), consistent with the sizes observed in our cryo-EM analysis. Complementing these findings, nanoparticle tracking analysis demonstrated that pEVs contained significantly higher particle concentrations (1.65×10^{12} particles/mL) (Fig. 1D). Having established the basic physical and morphological characteristics of our isolated pEVs, we selected heat-treated pellet platelet lysates (HPPL) as our comparative control for subsequent analyses. To

430 comprehensively compare these two platelet-derived preparations, we proceeded to analyze their
431 protein profiles, concentrations, and molecular signatures as detailed below.

432 We first examined the general protein profiles in both samples by SDS-PAGE. Analysis
433 under non-reducing and reducing conditions revealed distinct protein profiles between pEVs and
434 HPPL (Fig. 1E). Both conditions showed prominent bands around 60-65 kDa, likely corresponding
435 to protein disulfide isomerase or albumin in both samples. Under reducing conditions, additional
436 bands appeared: approximately 245 kDa in pEVs and 100-140 kDa in HPPL, possibly representing
437 integrin subunits. These distinct banding patterns suggest the presence of disulfide-dependent
438 protein complexes that are differentially distributed between these preparations. Total protein
439 quantification by BCA revealed comparable concentrations between pEVs (4.4 mg/mL) and HPPL
440 (5.9 mg/mL) preparations ($n=3$, $P > 0.05$; Fig. 1F), validating our subsequent comparative protein
441 profile analysis.

442 Having established the physical and basic protein characteristics of our preparations, we
443 proceeded to analyze specific markers to confirm the vesicular nature of our isolates. Surface
444 marker analysis using Exo-check demonstrated the presence of canonical EV markers in pEVs,
445 including tetraspanins (CD63, CD81), endosomal sorting proteins (TSG101), and membrane-
446 associated protein FLOT1 (Fig. 1G). Flow cytometry further confirmed the expression of CD9
447 (12.7%), a typical EV surface membrane marker, and platelet-specific marker CD41 (20.9%) (Fig.
448 1H), verifying that the pEVs retained markers related to their platelet origin.

449 To gain deeper insights into the molecular composition of our preparations, we also
450 conducted comprehensive proteomic analysis. LC-MS/MS analysis of the pEVs revealed a
451 proteome distinct from that of HPPL. Among the identified proteins, 313 were shared between the
452 two preparations, while 63 were unique to pEVs and 582 to HPPL (Fig. 1I). Notably,
453 approximately 39% of the pEV-specific proteins were immunoglobulins and about 12% were
454 complement-related proteins (Fig. 1J). The shared protein fraction between pEVs and HPPL also
455 showed significant differences in protein expression levels (Fig. 1K), with HPPL significantly
456 expressing proteins such as platelet-specific PF4, TGF-beta1, and CXCL7. Particularly significant
457 for potential therapeutic applications, approximately 1% of the pEV-specific proteome consisted

458 of extracellular matrix (ECM) and cell adhesion molecules (Fig. 1K), including CD44, LYVE1,
459 and HABP2 (Table S1).

460

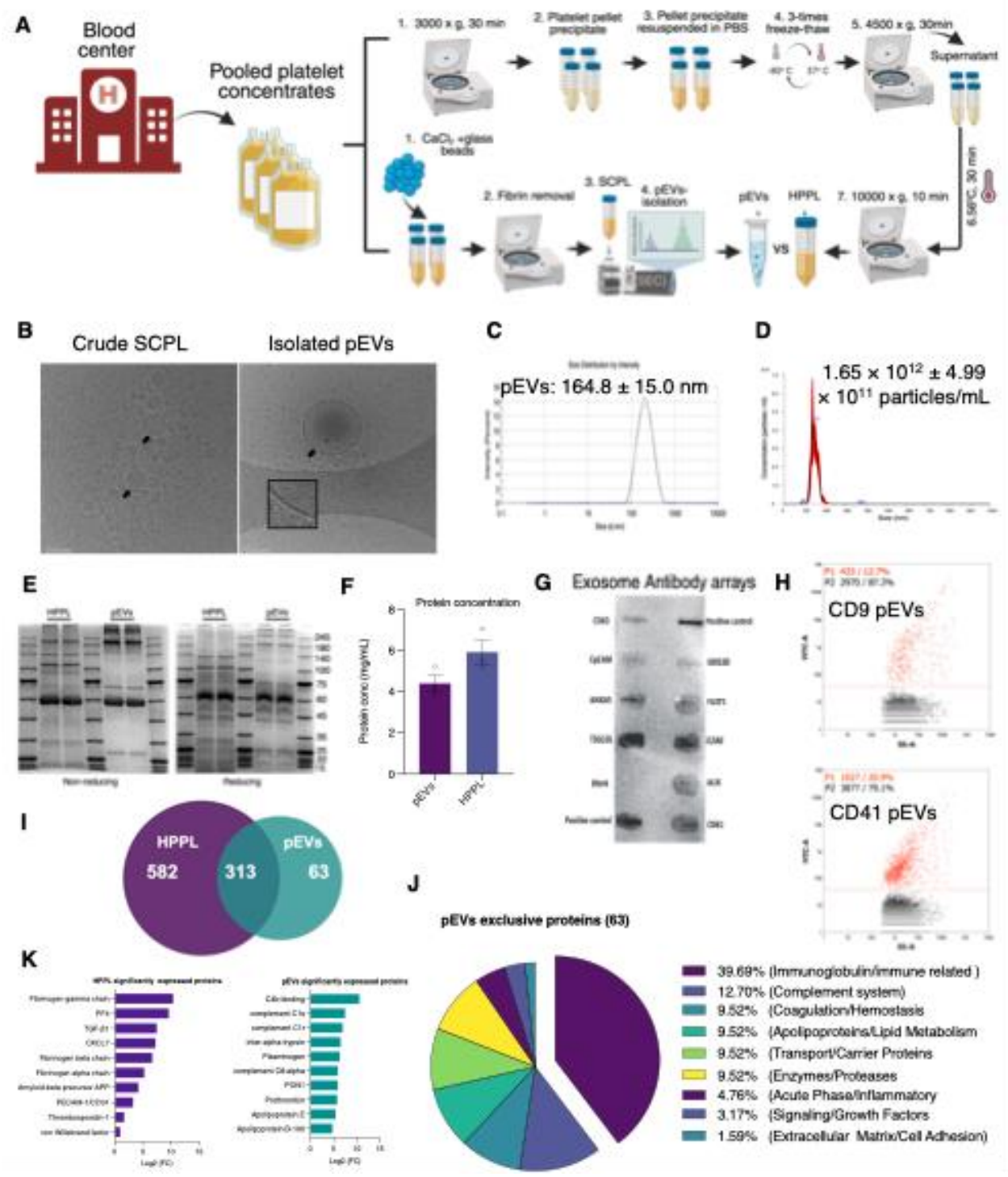

461

462 **Fig.1 Comprehensive characterization of platelet-derived extracellular vesicles (pEV) and**
463 **HPPL isolated from clinical-grade platelet concentrates. A.** Schematic workflow for isolation
464 and preparation of pEVs and HPPL from clinical-grade platelet concentrate. **B.** Representative
465 cryo-electron microscopy (cryo-EM) images showing EVs from SCPL (left) and SEC-isolated
466 EVs-SCPL (right). Arrows indicate characteristic double-membrane structure. Scale bar = 100 nm.
467 **C**. Size distribution profiles of pEVs determined by dynamic light scattering (DLS) across three
468 independent batches (mean ± SD, n = 3). **D**. Quantification of total particle yields from pEVs as
469 measured by nanoparticle tracking analysis (NTA). **E**. SDS-PAGE analysis of pEVs and HPPL
470 under reducing and non-reducing conditions (20 µg protein/lane). Molecular weight markers are
471 shown in the rightmost lane. **F.** Protein concentration are shown by BCA (n=3) **G**. Exo-Check
472 antibody array demonstrating expression of canonical EV markers (CD63, Tsg101, and CD81) in
473 pEVs. **H.** Nano flow cytometric analysis of CD9 and CD41 expression in pEVs at optimized
474 particle counts (2,000-12,000 particles/min), with size distribution and concentration determined
475 through software calibration. **I**. Venn diagram illustrating the proteomic profiles of pEVs and
476 HPPL, showing the number of shared and unique proteins identified in each preparation. **J**.
477 Functional categorization of proteins exclusively detected in pEVs, expressed as percentage
478 distribution across categories. **K**. Top 10 significantly enriched proteins in pEVs and HPPL,
479 ranked by expression ratio and quantified as log2 fold change (Log2FC) of pEVs versus HPPL.
480

481

482 *3.2. pEV selectively enhance neural precursor cell proliferation in the dentate gyrus*

483 To explore how pEVs and HPPL influence neural precursor cells, we focused on neurospheres
484 isolated from dentate gyrus (DG) of 8-week-old adult female mice. Using pooled cells from three
485 mice per region helped us minimize individual variations (Fig. 2A). Our initial investigation
486 examined whether supplementing the medium with pEVs and HPPL (0.5% v/v) could influence
487 neurosphere development. Interestingly, we found that pEVs specifically increased the size of DG
488 neurospheres without affecting their number (Fig. 2B). To further validate these distinct effects,
489 we examined neurosphere formation in the absence of exogenous growth factors. Notably, the
490 specific responses persisted under these stringent conditions, with pEVs continuing to selectively
491 enhance DG-derived neurosphere size (Fig. 2C). To assess treatment uptake by neurosphere cells,
492 we exposed them to Alexa Fluor 488-labeled pEVs and HPPL for 24 hours. Confocal microscopy
493 revealed progressive accumulation of fluorescent signal within neurospheres throughout this
494 period, demonstrating that neural progenitor cells efficiently internalize both pEVs and HPPL (Fig.
495 S1).

496 To corroborate our ex vivo findings, we tested pEVs-specific functions in the DG of
497 hippocampus in vivo. We administered pEVs, HPPL, or PBS (control) intranasally for three
498 consecutive days, along with daily EdU injections administered six hours apart from the intranasal

treatments to track newly dividing proliferating cells (Fig. 3A). Mice were sacrificed on day 4, and DG hippocampal tissue sections were analyzed for EdU staining. Quantification revealed significantly higher numbers of proliferating cells along the granular layer in pEVs-treated animals compared to controls (Fig. 3B), substantiating our ex vivo observations. These findings confirm that pEVs specifically enhance proliferation in the DG of the hippocampus.

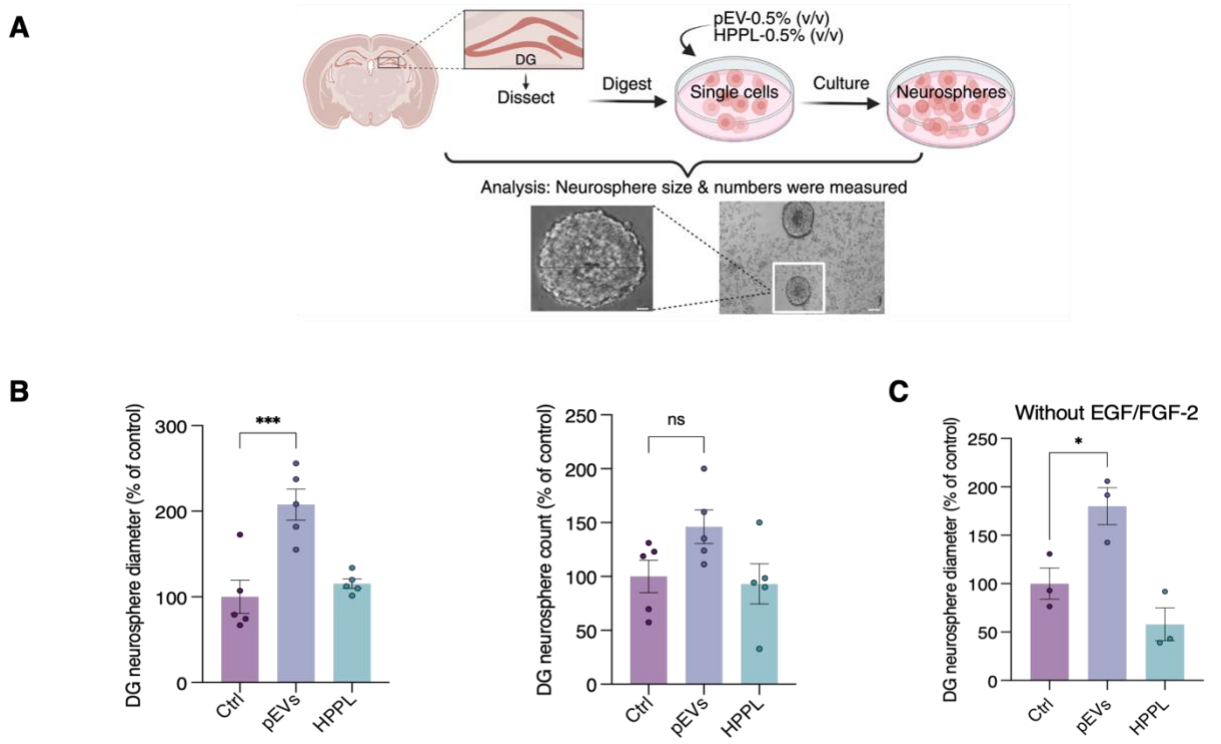

Fig.2 pEVs selectively regulate DG-derived neural precursor cell proliferation *ex vivo*. A. Schematic representation of neural stem cell isolation from the dentate gyrus (DG) followed by neurosphere generation. **B**. Quantification of neurosphere number and size distribution from DG-derived cultures following treatment with platelet concentrate-derived extracellular vesicles (pEVs) or heat-treated platelet pellet lysate (HPPL). The size of 50 neurospheres was analyzed per condition. For neurosphere number, all visible neurospheres were counted in 80 wells of a 96-well plates per condition. Data are mean ± SEM from five independent experiments. ***$p < 0.001$ vs PBS using one-way ANOVA followed by Dunnett's multiple comparisons post-hoc test. Control condition is normalized to 100%, and that pEVs and HPPL values represent the relative change in neurosphere size and number compared to this baseline. **C.** Proliferation of DG-derived neurospheres treated with pEVs or HPPL in the absence of EGF and FGF-2. Data represent mean ± SEM from three independent experiments. $p < 0.05$ by one-way ANOVA with multiple comparisons.

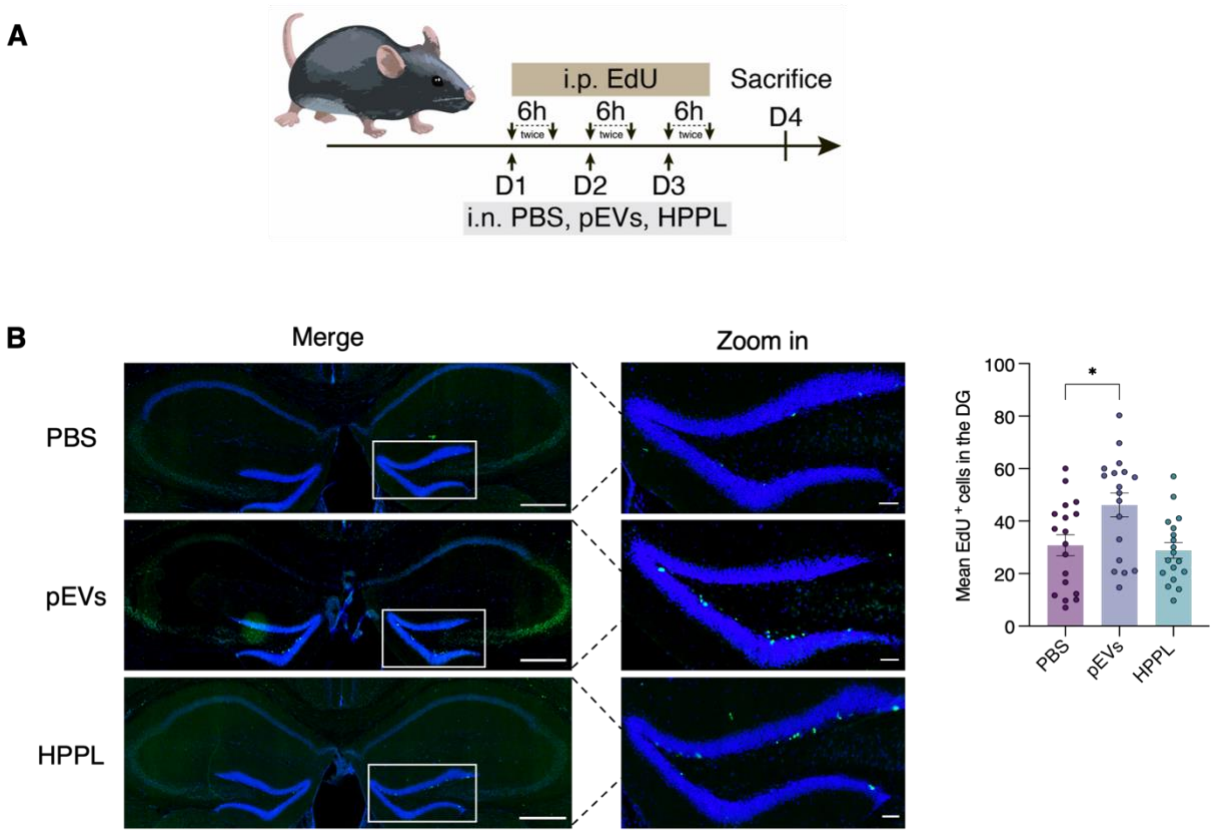

Fig.3 pEVs selectively regulate DG neural precursor cell proliferation *in vivo* at day 3. **A.** Schematic representation of the short-term (3-day) intranasal delivery protocol for pEVs or HPPL, combined with EdU (50 mg/kg) i.p administration twice daily at 6-hour intervals. **B.** Representative confocal images of EdU^+ cells in the DG following 3-day treatment with pEVs or HPPL. Green channel represents EdU-labeled cells, and blue channel shows DAPI nuclear staining. Images acquired by Stellaris confocal microscopy with (20× objectives). Scale bar: 100 µm (inset: 50 µm). Quantification of total EdU^+ cells across 5 DG sections/animal along the granular layer in DG. Data are mean ± SEM (N = 18 animals per group). *$p < 0.05$ vs PBS using one-way ANOVA followed by Dunnett's multiple comparisons post-hoc test.

3.3. pEVs and HPPL Exert Divergent Effects on Neural Precursor Cell Differentiation

To further analyze how pEVs influence the cell fate of ex vivo neuronal precursor cells, we evaluated differentiation patterns of second-passage neurospheres from the dentate gyrus treated with pEVs or HPPL (0.5% v/v) for 10 days (Fig. 4A). At the end of the incubation period, we stained the DG-derived neurospheres with markers for immature neurons (DCX^+) and mature neurons ($NeuN^+$). Interestingly, HPPL treatments significantly promoted differentiation into

539 immature DCX$^+$ neuroblasts (Fig. 4B-C). In contrast, pEVs treatment significantly induced
540 differentiation of neural precursor cells into mature NeuN$^+$ neurons rather than immature DCX$^+$
541 neuroblasts (Fig. 4B-D).

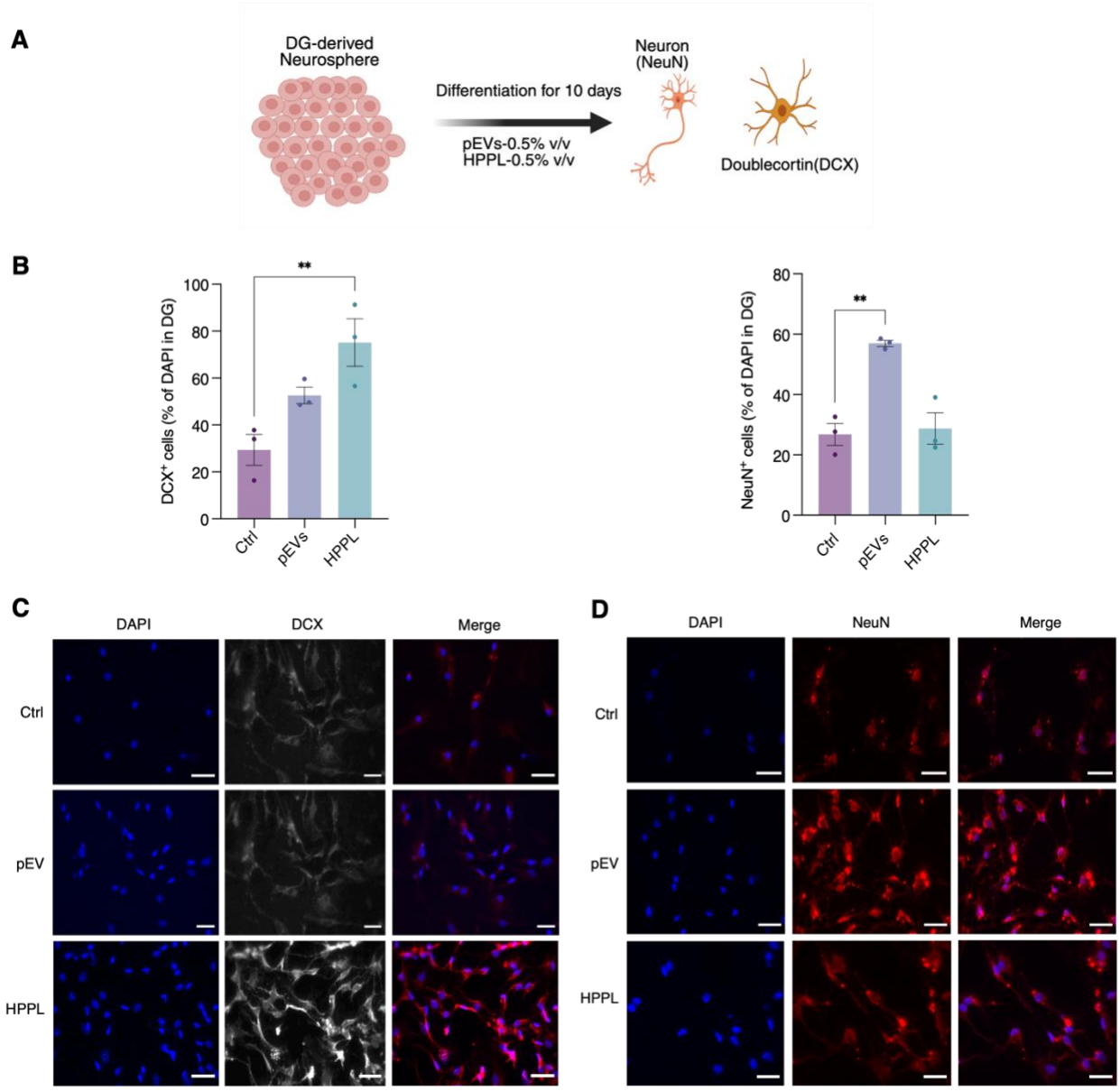

542

543 **Fig.4 Differentiation of neural precursor cells ex vivo under pEV and HPPL stimulation A.**
544 Schematic representation of the experimental design for neurosphere differentiation studies under
545 pEVs and HPPL conditions. **B.** Quantification of DCX, and NeuN-positive cells as a percentage
546 of total DAPI-positive nuclei per field. Data represent mean ± SEM from (n=3) ordinary one-way
547 ANOVA followed by Dunnett's (**$p < 0.01$) with multiple comparisons post-hoc test. **C.**
548 Representative immunocytochemistry images showing DCX expression (red) in differentiated
549 neurospheres under pEVs or HPPL treatment compared to untreated controls. Nuclei

550 counterstained with DAPI (blue) Scale bars = 50µm **D.** Representative immunocytochemistry
551 images of DG-derived differentiated neurospheres immunostained for NeuN (red) following pEV
552 or HPPL treatment versus untreated controls. Nuclei counterstained with DAPI (blue) Scale bars
553 = 50µm.

554

555 *3.4. Long-term assessment of hippocampal neurogenesis in the dentate gyrus under pEV*

556 To investigate the long-term neurogenic effects of platelet-derived extracellular vesicles (pEVs)
557 and heat-treated platelet pellet lysates (HPPL), a separate cohort of mice received intranasal
558 administration of either pEVs or HPPL three times per week over a 28-day period. To trace
559 dividing cells, 5-ethynyl-2′-deoxyuridine (EdU) was administered during the first three days of
560 treatment (Fig. 5A). This strategy allowed the identification of cells that entered the cell cycle
561 early during the treatment window.

562 At the end of the 28-day treatment, immunohistochemistry revealed a significant increase
563 in the total number of EdU^+ cells in the dentate gyrus (DG) of HPPL-treated mice (Fig. 5B-C),
564 suggesting enhanced cellular proliferation and/or survival. Moreover, a notable increase in the
565 proportion of EdU^+ cells co-expressing doublecortin (DCX), a marker of immature neurons, was
566 observed in the HPPL group. This indicates that HPPL not only boosts proliferation but may also
567 promote early neurogenic differentiation.

568 While pEV-treated mice showed a trend toward an increase in total EdU^+ cells, this change
569 was not statistically significant (Fig. 5B-D). However, pEV treatment significantly elevated the
570 proportion of EdU^+ cells that co-expressed NeuN, a marker of mature neurons, within the DG
571 granule cell layer. This suggests that pEVs may facilitate the maturation and survival of newborn
572 neurons over time.

573

574

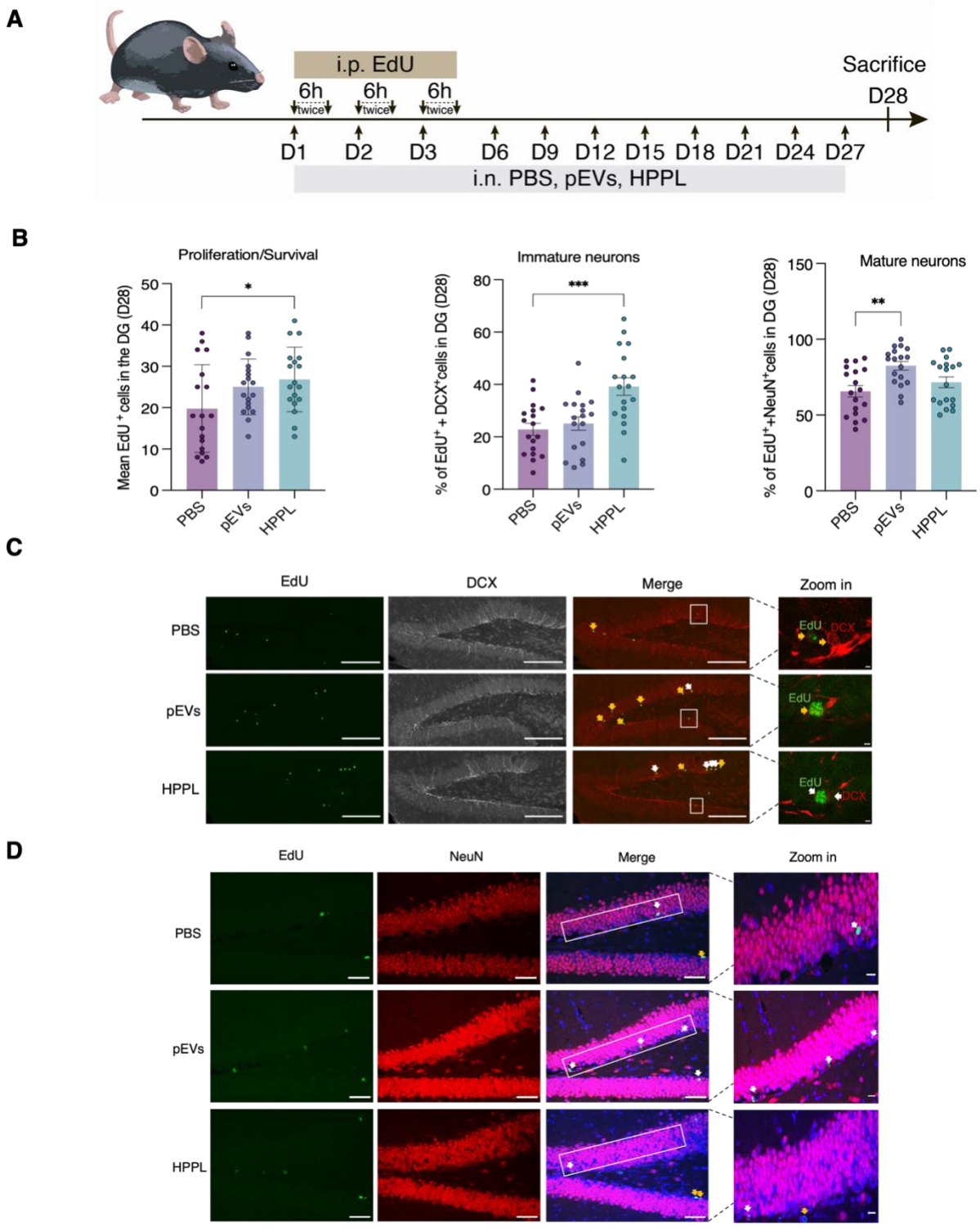

Fig.5 pEVs promote neurogenesis in the dentate gyrus (DG) of hippocampus. **A.** Experimental design schematic showing long-term (28-day) intranasal administration protocol for pEVs and HPPL combined with EdU (50 mg/kg) labeling regimen (twice daily at 6-hour intervals). **B.** Quantification shows total EdU^+ cells across 5 DG sections/animal along the granular layer in DG,

580 percentage of co-expressing DCX^+/EdU^+ and $NeuN^+/EdU^+$ cells in the granular layer of DG region.
581 Data represent mean ± SEM (N = 18 animals per group). Statistical significance determined by
582 ordinary one-way ANOVA followed by Dunnett's (*p < 0.05, **p < 0.01 ***$p < 0.001$) *with*
583 *multiple comparisons post-hoc test.* **C-D.** Representative images of immature/mature neurons co-
584 expressing DCX^+/EdU^+ and $NeuN^+/EdU^+$ in the granular layer of DG following pEVs & HPPL
585 treatment at day 28. DCX is illustrated by gray channel, EdU by green channel, and NeuN, by red
586 channel. Scale bars: 50 µm; inset scale bar: 20 µm. White arrows indicate DCX^+/EdU^+, and
587 $NeuN^+/EdU^+$ co-expressing cells, orange arrows indicate DCX^-/EdU^+, and $NeuN^-/EdU^+$ cells.
588 Representative images were captured using Stellaris confocal microscopy with (63× objectives).
589 Data indicate that pEVs significantly increase the proportion of $NeuN^+$ cells among EdU^+ cells in
590 the DG, suggesting enhanced neuronal differentiation, while HPPL primarily promotes cell
591 proliferation and increases the number of immature neurons in the DG.

592

593 *3.5. Proteomic Insights into pEV-mediated modulation of dentate gyrus neurogenesis*
594

595 To unveil the mechanisms underlying the effects of pEVs on dentate gyrus of hippocampal
596 neurogenesis, we performed a proteomic analysis of DG tissue following 28 days of intranasal
597 pEV or PBS treatment (N = 2 per group; Fig. 6A). 2,656 proteins were identified in the pEV group
598 versus 2,629 in the PBS group, with 2,580 proteins (95.4%) shared. 76 proteins were unique to
599 pEV-treated tissue, and 49 to PBS (Fig. 6B). GO-term analysis of the 76 pEV-specific proteins in
600 DG tissue showed enrichment in protein binding and cell adhesion molecule binding functions
601 (Table S2; Fig. S2). Differential proteomic analysis identified 111 significantly regulated proteins,
602 with 61 upregulated and 50 downregulated (Fig. 6C). The upregulated proteins were primarily
603 associated with biological processess of CNS myelination, oxygen binding, and postsynaptic
604 signaling, and were enriched in oxidative phosphorylation and neuroplasticity-related KEEG
605 pathways (Fig. 6D, red). The most profoundly altered proteins following pEV treatment are
606 detailed in (Table S3). Among the significantly upregulated proteins, several key regulators of
607 neurogenesis emerged with angiotensin-converting enzyme (ACE; Log_2FC: 1.6537), which
608 suggests altered regulation of the renin-angiotensin system. Structural neuronal proteins were also
609 elevated, such as internexin neuronal intermediate filament protein Alpha (INA; Log_2FC: 1.0899)
610 and developmentally regulated GTP-binding Protein 1 (DRG1; Log2FC: 1.2182). Additionally,
611 proteins associated with neuronal maturation, including Ras-related protein Rab-7a (RAB7;
612 Log_2FC: 0.917) and brain abundant membrane-attached signal protein 1 (BASP1; Log_2FC: 0.7989)
613 were upregulated (Fig. 6D). In contrast, downregulated proteins were predominantly enriched in

614 biological processes related to cytoplasmic translation, actin filament organization, and cell
615 migration (Fig. 6D, blue). They included key cytoskeletal regulators such as Rho-associated
616 coiled-coil containing protein kinase 1 (ROCK1; Log2FC: -0.7107), known for its role in actin
617 dynamics and cell proliferation [38], as well as stathmin 1 (STMN1), a regulator of microtubule
618 stability, and Ras-related C3 botulinum toxin substrate 1 (RAC1), a GTPase involved in
619 lamellipodia formation. The reduced expression of these proteins suggests diminished migratory
620 activity as neurons settle into their final positions. Ingenuity Pathway Analysis (IPA) confirmed
621 activation of respiratory electron transport, myelination, and ubiquitination pathways (Fig. 6E).
622 IPA also uniquely identified activation of Notch4 signaling, critical for neural stem cell
623 maintenance [39] and MHC class I antigen presentation, suggesting coordinated neurogenic and
624 immune-related responses following pEV treatment. Our molecular analyses revealed distinct
625 biological pathways affected by the treatments. Expanded protein-protein interaction (PPI)
626 analysis further corroborated these findings, with upregulated proteins distinctly clustering in
627 myelination and proteasome pathways, while downregulated proteins were predominantly
628 associated with translation processes. The comprehensive network visualization and analysis of
629 these interactions is presented in (Fig. 7A-B), providing a systems-level perspective that integrates
630 our findings.

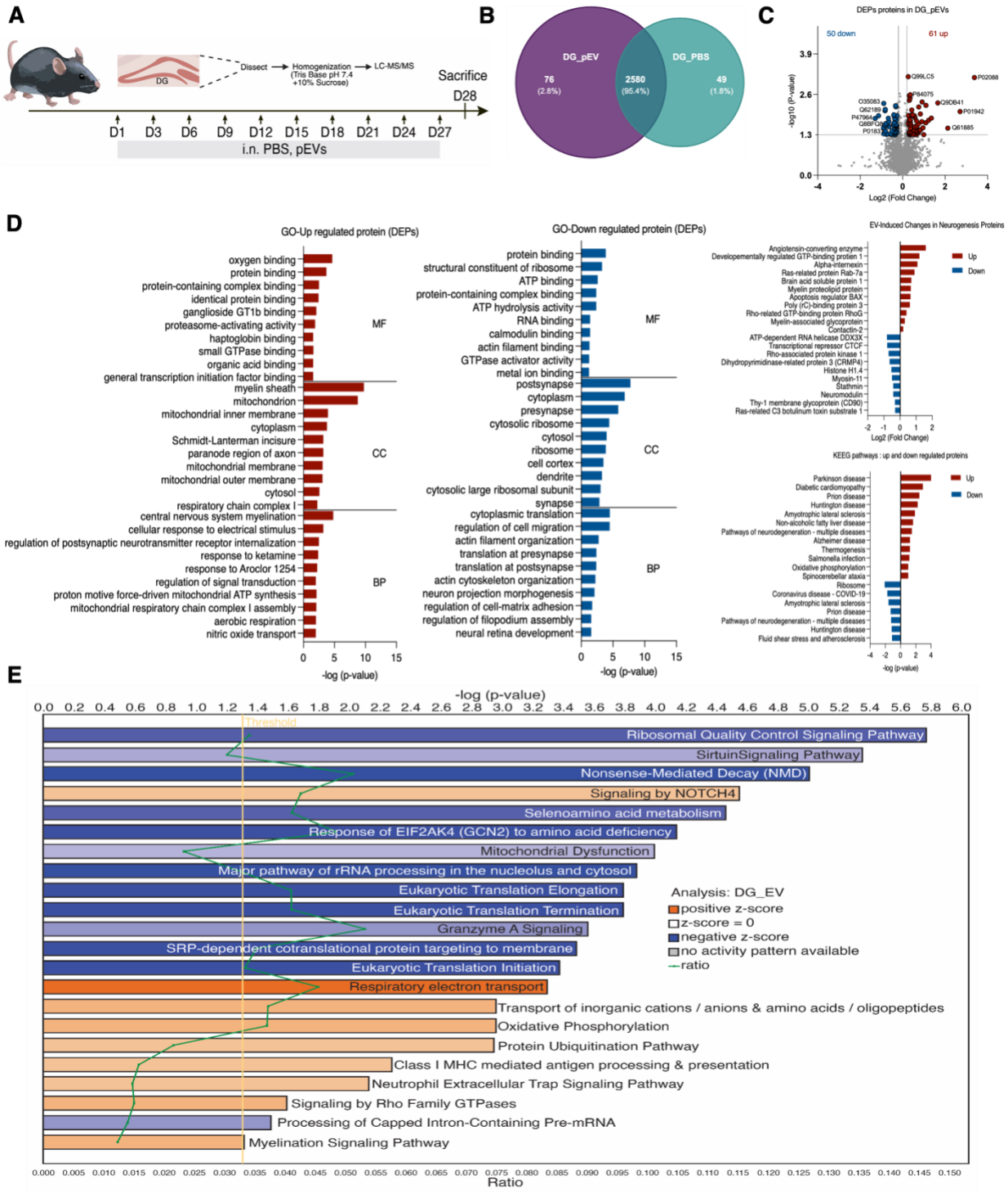

Fig.6 Proteomic profiling reveals pEVs-induced molecular changes in the dentate gyrus (DG) of hippocampus. A. Experimental workflow showing DG tissue collection following 28-day of intranasal administration of pEVs or PBS as control, followed by proteomic profiling via LC-MS/MS. **B.** Venn diagram illustrating the overlap of identified proteins in DG tissue from pEVs and PBS-treated groups, highlighting both shared and treatment-specific proteins. **C.** The

differentially expressed proteins (DEPs) were identified by comparing proteins commonly expressed between pEV-treated samples and PBS controls. Volcano plot analysis of these DEPs in DG tissue following pEV treatment revealed significant changes using thresholds of $p \leq 0.05$ and fold change ≥ 1.2. Red and blue points on the plot indicate significantly upregulated and downregulated proteins, respectively. **D.** Gene Ontology (GO) enrichment of upregulated and downregulated DEPs categorized by biological process, molecular function, and cellular component. Neurogenesis Pathway Proteins Altered by EV Treatment: Upregulated and Downregulated Proteins with Log2FC Values, KEGG pathway analysis is shown for both subsets. **E.** Canonical pathway analysis of differentially expressed proteins (DEPs) using Ingenuity Pathway Analysis (IPA), highlighting significantly altered signaling networks ($p < 0.05$) after DG_EV treatment compared to PBS. Pathways are color-coded by activation z-score: orange bars indicate predicted activation (positive z-score), blue bars indicate predicted inhibition (negative z-score), and white bars indicate pathways with z-score = 0. The green line represents the ratio of DEPs present in each pathway relative to the total proteins in that pathway.

A Upregulated proteins in the dentate gyrus (DG) under pEVs treatment and their protein-protein interactions (PPI)

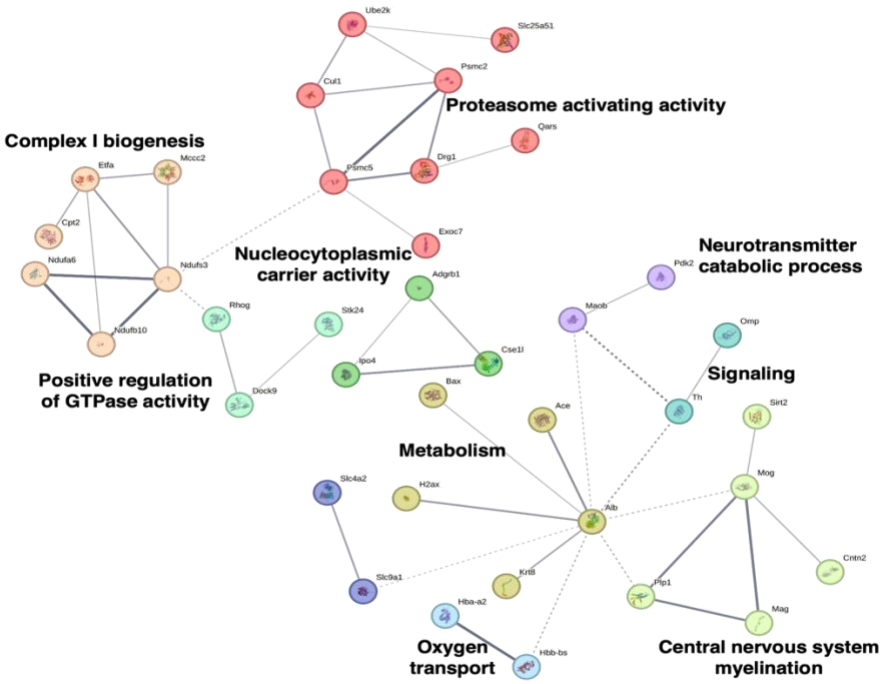

B Down regulated proteins in the dentate gyrus (DG) under pEVs treatment and their protein-protein interactions (PPI)

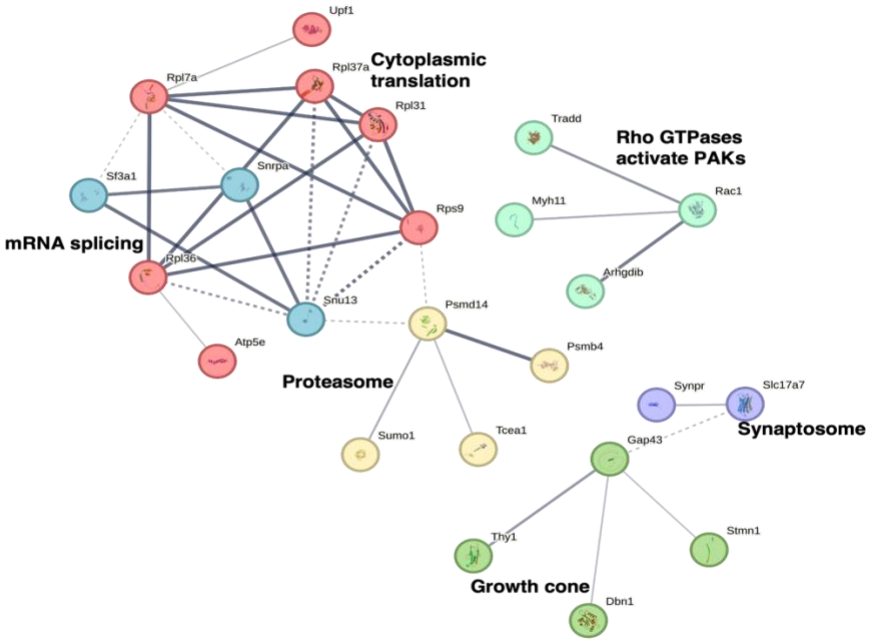

652

Fig.7 STRING protein-protein interaction network analysis of upregulated and downregulated proteins in DG following pEVs treatment. A. Network was generated using MCL clustering algorithm with inflation parameter of 3 to identify natural clusters based on stochastic flow. Network statistics: 61 nodes (proteins), 45 edges (interactions), average node degree of 1.48, and average local clustering coefficient of 0.423. The network shows significant enrichment in protein-protein interactions (PPI enrichment p-value: 0.000114) compared to expected interactions (24). Visualization parameters: maximum FDR ≤ 0.05, minimum signal ≥ 0.01, and minimum interaction strength ≥ 0.01. **B**. Network was generated using MCL clustering algorithm with inflation parameter of 3 to identify natural clusters based on stochastic flow. Network statistics: 50 nodes (proteins), 34 edges (interactions), average node degree of 1.36, and average local clustering coefficient of 0.344. The network shows significant enrichment in protein-protein interactions (PPI enrichment p-value: 0.02) compared to expected interactions (23). Visualization parameters: maximum FDR ≤ 0.05, minimum signal ≥ 0.01, and minimum interaction strength ≥ 0.01.

4. Discussion

This study provides new insights into the use of pEVs as bioactive, cell-free materials able to modulate adult hippocampal neurogenesis. Using ex vivo neurosphere cultures and in vivo intranasal delivery in adult mice, we demonstrate that pEVs selectively enhance proliferation and maturation of DG neural precursor cells. Our proteomic analysis reveals that pEVs modulate hippocampal protein expression in pathways related to mitochondrial function, myelination, and immune signaling. These findings support the translational potential of pEVs as a next-generation neurorestorative therapy for age-related and neurodegenerative brain disorders.

Previous studies have demonstrated the neuroprotective potential of HPLs administered via intranasal route in rodent models of Parkinson's disease [21, 23] and Alzheimer's disease [24], via intracerebroventricular injection in models of amyotrophic lateral sclerosis (ALS) [22], and directly applied to the brain surface in models of traumatic brain injury (TBI) [20]. These beneficial effects have been linked to the rich content of trophic factors (e.g. BDNF, VEGF, PDGF, PF4) [21, 22] and functional biomolecules such as antioxidants [40, 41], which protect against various forms of cell death and oxidative stress. HPLs consistently outperform standard recombinant growth factors, with their protective effects involving Akt pathway activation and context-dependent involvement of MEK signaling [42]. pEVs represent a more defined fraction enriched in membrane-enclosed cargo and free from large plasma proteins, likely enabling better mechanistic

688 clarity, and, possibly, reproducibility [14, 43]. The current study builds on this rationale by directly
689 comparing pEVs with a benchmark neuroprotective lysate, HPPL [21].
690 The DG of the adult hippocampus is a key site of lifelong neurogenesis in adults, providing
691 holistic roles in learning and memory [44] but is highly sensitive to aging and disease [45]. Our
692 ex vivo and in vivo findings show that, as compared to HPPL, pEVs enhance proliferation of DG-
693 derived neural progenitors ex vivo, even in the absence of EGF and FGF-2, suggesting intrinsic
694 trophic effects. Neural progenitor cell fate also differed markedly between treatments with both
695 platelet biomaterials. Indeed, pEVs directed differentiation toward mature $NeuN^+$ neurons, while
696 HPPL only promoted development of immature neuronal cells in both neurosphere ex vivo
697 analysis and in vivo. Overall, our data demonstrate that pEVs exert a powerful impact on DG
698 neurogenesis, significantly influencing both proliferation and differentiation processes. This
699 comprehensive effect underscores the potential of pEVs as modulators of adult hippocampal
700 neurogenesis across multiple stages of neural development
701 Interestingly, our DG proteomic finding revealed the complex molecular landscape
702 underlying pEV-mediated neurogenic effects in the dentate gyrus, suggesting a sophisticated
703 interplay between neurodevelopmental regulators and immunomodulator factors. The
704 upregulation of key neurogenic regulators in DG tissue including ACE (modulating angiotensin
705 signaling for progenitor proliferation)[46], INA and BASP1 (orchestrating cytoskeletal
706 organization and transcriptional reprogramming) [47], DRG1 (coordinating GTPase activity for
707 neuronal migration) [48], and RAB7 (optimizing endosomal trafficking for synaptogenesis) [49]
708 reveals that pEV treatment induces a sophisticated protein expression profile that simultaneously
709 influences multiple critical neurogenic processes from neural stem cell activation through terminal
710 differentiation, ultimately favoring the development of mature $NeuN^+$ neurons over immature
711 neuroblasts. Simultaneously, the downregulation of cytoskeletal restrictors including ROCK1
712 (inhibitor of neurite outgrowth and branching)[50], RAC1 (controller of actin cytoskeleton
713 dynamics) [51], and STMN1 (microtubule destabilizing protein) [52]. While these proteins are
714 typically essential for various aspects of neuronal development, their downregulated expression in
715 this context occurring alongside upregulation of key neurogenic factors would indicate a
716 coordinated remodeling of the cytoskeletal regulatory network. This appears to create a precisely
717 balanced neurogenic environment in response to our treatment, rather than simple inhibition of
718 these pathways.

719 Further supporting these findings, IPA analysis revealed activation of Notch4 and MHC
720 class I-related pathways, which is consistent with emerging evidence that Notch signaling plays a
721 dual role in adult neurogenesis by maintaining the neural stem cell pool while directing lineage
722 commitment toward neuronal fates [53, 54]. The concurrent activation of MHC class I-related
723 pathways suggests pEVs create an immune-privileged microenvironment that would protect
724 developing neurons during their vulnerable integration period [55-57]. This molecular signature
725 represents a sophisticated regulatory network that balances stem cell maintenance with neuronal
726 differentiation while simultaneously modulating neuroinflammatory processes known to influence
727 the neurogenic niche. Collectively, these complementary mechanisms establish the molecular
728 foundation underlying pEV-mediated neurogenic enhancement, particularly explaining the
729 preferential generation of mature $NeuN^+$ neurons observed consistently across our ex vivo and in
730 vivo analyses. The EV proteome also included ECM-binding proteins (e.g., CD44, LYVE1,
731 HABP2), which are known to interact with hyaluronan, a key ECM component known to regulate
732 neural stem cell maintenance and proliferation, suggesting potential mechanisms for the biological
733 effects of pEVs in neural tissue applications [58].
734 Immunoregulatory components (e.g., complement proteins, Ig fragments) were also
735 detected in the EV proteome pointing to a potential role in remodeling the neurogenic niche. These
736 immune-related factors may contribute to the creation of a permissive microenvironment by
737 modulating local inflammatory processes [59], clearing cellular debris, and regulating microglial
738 activation states. The complement proteins present in our EVs, particularly C4b, may engage with
739 complement receptors on neural cells [60], potentially influencing cellular recognition, synaptic
740 refinement, and microglial activity in ways that ultimately promote neurogenesis [61]. This finding
741 adds to the growing evidence that immune-related molecules play non-canonical roles in neural
742 development and plasticity, extending beyond their traditional immune functions [62].
743 Additionally, the identified immunomodulatory factors could regulate the cross-talk between
744 neural and immune cells within the neurogenic niche [63], potentially suppressing detrimental pro-
745 inflammatory signals while enhancing trophic support [64].
746 The pEVs used in this study were isolated from serum-converted platelet lysates using
747 similar GMP-compatible SEC method as previously described in a cardiac ischemia/reperfusion
748 [29]. In the cardiac ischemia study, SCPL-EVs improved cardiac function, reduced apoptosis and
749 scarring, and promoted angiogenesis, with no adverse coagulation or systemic toxicity effects [29].

750 These data confirm the functional activity and safety of SCPL-EVs across tissues. Proteomic
751 features such as the enrichment of HSP70, RAP1B, and LGALS3BP, and the depletion of
752 coagulation-related proteins, were consistent across this and our study. Additional support for the
753 translational versatility of pEVs comes from their successful use in ocular models [13]. A separate
754 study from our group demonstrated that pEVs, isolated from PC supernatants by
755 ultracentrifugation, efficiently delivered the anti-angiogenic agent kaempferol to the cornea,
756 suppressed pathological neovascularization, and extended drug retention on the ocular surface [31]
757 while also exerting its own beneficial biological effects in this application. This work highlighted
758 the intrinsic anti-inflammatory and targeting properties of pEVs, and their capacity to modulate
759 angiogenic and inflammatory gene expression in vascular endothelial cells. The ability of native
760 pEVs to penetrate tissue barriers and enhance therapeutic retention further reinforces their
761 relevance as delivery vectors for CNS therapies, where barrier crossing and local retention are
762 critical [13, 27]. Furthermore, previous investigations from our group using fluorescently labeled
763 HPPL and pEVs demonstrated that proteins from these materials can diffuse into the brain and
764 reach the hippocampus following intranasal administration in mice [19, 40]. These findings
765 therefore support the feasibility of delivering bioactive platelet-derived molecules, including those
766 packaged in pEVs, to central brain regions through the intranasal route. Additional evidence for
767 the therapeutic value of SCPL-EVs also comes from a recent study demonstrating their successful
768 integration into gelatin-based hydrogel foams for wound healing applications [32]. In this model,
769 the same type of pEVs as used in the current manuscript was incorporated into engineered
770 hydrogels and applied to chronic wounds in diabetic rats. The formulation not only accelerated
771 wound closure but also modulated macrophage polarization, promoted angiogenesis, and
772 maintained a low-inflammatory environment [32]. These effects were consistent with the anti-
773 inflammatory and pro-regenerative activity observed in the brain and reinforce the multifunctional
774 capacity of pEVs to modulate both immune and tissue repair responses. The biocompatibility and
775 safety of pEVs in this context further support their translation toward clinical applications in tissue
776 regeneration, including CNS repair. Together, these findings support the use of pEVs as a well-
777 characterized, reproducible, and scalable biomaterial for brain repair. Importantly, while this study
778 emphasizes the distinct advantages of pEVs, it also confirms the functional activity of HPPL,
779 which significantly enhanced the pool of immature neural progenitors both ex vivo and in vivo.
780 This complementary effect suggests that HPPL may support early stages of neurogenesis, while

781 pEVs promote later maturation. These observations raise the possibility that a combined
782 therapeutic approach, leveraging both HPPL and pEVs, could provide additive or synergistic
783 benefits across multiple stages of neural regeneration. Future studies should explore this
784 hypothesis experimentally to optimize platelet-derived therapies for CNS repair. The consistent
785 efficacy of PC-derived EVs in both cardiac and neural injury models, and promising performance
786 in ocular delivery, highlights their broad regenerative potential and encourages further exploration
787 for clinical applications in neurological diseases.

788 In conclusion, the ability of pEVs to modulate neuronal maturation and engage immune
789 and metabolic pathways opens new avenues for non-cell-based interventions in neurodegenerative
790 disease. Their compatibility with minimally invasive delivery (e.g., intranasal) and scalable
791 production from clinical-grade PC [13] makes them attractive for translational development.
792 Future work should assess long-term behavioral outcomes, explore their efficacy in aging and
793 disease models, and dissect the contribution of specific vesicular components to neurogenesis and
794 synaptic plasticity. Overall, this study advances the concept that extracellular vesicles derived from
795 human platelet concentrates constitute a novel and versatile neuroregenerative platform with
796 potential clinical utility.
797

798 **Funding sources**

799 This research was supported by grants from the National Science and Technology Council (NSTC
800 113-2923-E-038-001), the National Health Research Institutes (NHRI-EX114-11431NI), Taiwan,
801 and the WILL Chair France 2023 to TB, and the NSTC 114 -2927-I-038 -504 -/Inserm grant to
802 DB and TB. AN was supported by a 2-years PhD fellowship from Taipei Medical University, TB
803 lab funding, and a MobLilex travel grant from ULille.
804

805 **CRediT authorship contribution statement**

806 AN performed the experiments, analyzed the data and drafted the manuscript. LNTN conducted
807 the proteomics analysis. ON performed part of the intranasal administrations at Lille University.
808 EF assisted with the analysis of the brain sections. LD assisted with intranasal administration and
809 mouse sacrifice procedures at TMU. MC assisted in proteomics data interpretation and design of
810 figures. JL performed parallel ex vivo neurosphere assays using platelet lysates and discussed data.
811 KB suggested and provided recommendations for the ex vivo neurosphere assays. LB contributed

to methodological recommendations and funding. TLW provided expert recommendations all along the study, conducted data analysis, and drafted the manuscript. DB and TB are PhD co-advisors of AN, conceived the study design, provided funding support, and drafted the manuscript. All authors revised and approved the final version.

Declaration of competing interest

MLC and TB are co-inventors of patents owned by Taipei Medical University. TB is co-founder of a start-up (Invenis Biotherapies) on platelet lysates to treat neurological disorders. The other authors declare no competing financial interest.

Data availability

Data will be made available on request.

Acknowledgments

We thank the Taipei Blood Center (Guangdu, Taiwan) for supplying the platelet concentrates and the Consortia of Key Technologies and Instrumentation Center at National Taiwan University for providing mass spectrometry technical services for brain tissue analysis.

Appendix A. Supplementary data

References

[1] P.-M. Lledo, M. Alonso, M.S. Grubb, Adult neurogenesis and functional plasticity in neuronal circuits, Nature Reviews Neuroscience 7(3) (2006) 179-193.
[2] M.P. Jurkowski, L. Bettio, E. K. Woo, A. Patten, S.-Y. Yau, J. Gil-Mohapel, Beyond the Hippocampus and the SVZ: Adult Neurogenesis Throughout the Brain, Frontiers in Cellular Neuroscience Volume 14 - 2020 (2020).
[3] H.S. Ghosh, Adult Neurogenesis and the Promise of Adult Neural Stem Cells, J Exp Neurosci 13 (2019) 1179069519856876.
[4] C. Anacker, R. Hen, Adult hippocampal neurogenesis and cognitive flexibility—linking memory and mood, Nature Reviews Neuroscience 18(6) (2017) 335-346.
[5] M. Alonso, A.-C. Petit, P.-M. Lledo, The impact of adult neurogenesis on affective functions: of mice and men, Molecular Psychiatry 29(8) (2024) 2527-2542.

[6] T. Elliott, K.Y. Liu, J. Hazan, J. Wilson, H. Vallipuram, K. Jones, J. Mahmood, G. Gitlin-Leigh, R. Howard, Hippocampal neurogenesis in adult primates: a systematic review, Molecular Psychiatry 30(3) (2025) 1195-1206.
[7] L. Culig, X. Chu, V.A. Bohr, Neurogenesis in aging and age-related neurodegenerative diseases, Ageing research reviews 78 (2022) 101636.
[8] F. Ávila-Gámiz, A.M. Pérez-Cano, J.M. Pérez-Berlanga, R.M. Mullor-Vigo, E.N. Zambrana-Infantes, L.J. Santín, D. Ladrón de Guevara-Miranda, Sequential treadmill exercise and cognitive training synergistically increase adult hippocampal neurogenesis in mice, Physiology & Behavior 266 (2023) 114184.
[9] O. Leiter, S. Seidemann, R.W. Overall, B. Ramasz, N. Rund, S. Schallenberg, T. Grinenko, B. Wielockx, G. Kempermann, T.L. Walker, Exercise-Induced Activated Platelets Increase Adult Hippocampal Precursor Proliferation and Promote Neuronal Differentiation, Stem Cell Reports 12(4) (2019) 667-679.
[10] G.D. Clemenson, W. Deng, F.H. Gage, Environmental enrichment and neurogenesis: from mice to humans, Current Opinion in Behavioral Sciences 4 (2015) 56-62.
[11] O. Leiter, D. Brici, S.J. Fletcher, X.L.H. Yong, J. Widagdo, N. Matigian, A.B. Schroer, G. Bieri, D.G. Blackmore, P.F. Bartlett, V. Anggono, S.A. Villeda, T.L. Walker, Platelet-derived exerkine CXCL4/platelet factor 4 rejuvenates hippocampal neurogenesis and restores cognitive function in aged mice, Nat Commun 14(1) (2023) 4375.
[12] M. Vassal, F. Martins, B. Monteiro, S. Tambaro, R. Martinez-Murillo, S. Rebelo, Emerging Pro-neurogenic Therapeutic Strategies for Neurodegenerative Diseases: A Review of Pre-clinical and Clinical Research, Molecular Neurobiology 62(1) (2025) 46-76.
[13] T. Burnouf, M.L. Chou, D.J. Lundy, E.Y. Chuang, C.L. Tseng, H. Goubran, Expanding applications of allogeneic platelets, platelet lysates, and platelet extracellular vesicles in cell therapy, regenerative medicine, and targeted drug delivery, J Biomed Sci 30(1) (2023) 79.
[14] J. Johnson, Y.W. Wu, C. Blyth, G. Lichtfuss, H. Goubran, T. Burnouf, Prospective Therapeutic Applications of Platelet Extracellular Vesicles, Trends Biotechnol 39(6) (2021) 598-612.
[15] R.P. Carney, R.R. Mizenko, B.T. Bozkurt, N. Lowe, T. Henson, A. Arizzi, A. Wang, C. Tan, S.C. George, Harnessing extracellular vesicle heterogeneity for diagnostic and therapeutic applications, Nature Nanotechnology 20(1) (2025) 14-25.
[16] D. Li, L.-T. Huang, C.-p. Zhang, Q. Li, J.-H. Wang, Insights Into the Role of Platelet-Derived Growth Factors: Implications for Parkinson's Disease Pathogenesis and Treatment, Frontiers in Aging Neuroscience Volume 14 - 2022 (2022).
[17] D. Duerschmied, E. Mammadova-Bach, M. Mauler, A. Braun, Immuno-Thrombotic Effects of Platelet Serotonin, in: K. Fatima-Shad (Ed.), Serotonin - A Chemical Messenger Between All Types of Living Cells, IntechOpen, Rijeka, 2017.
[18] Y. Hayon, O. Dashevsky, E. Shai, D. Varon, R.R. Leker, Platelet lysates stimulate angiogenesis, neurogenesis and neuroprotection after stroke, Thromb Haemostasis 110(2) (2013) 323-330.
[19] L. Delila, O. Nebie, N.T.N. Le, K. Timmerman, D.-Y. Lee, Y.-W. Wu, M.-L. Chou, L. Buée, S.-Y. Chou, D. Blum, D. Devos, T. Burnouf, Neuroprotective effects of intranasal extracellular vesicles from human platelet concentrates supernatants in traumatic brain injury and Parkinson's disease models, Journal of Biomedical Science 31(1) (2024) 87.
[20] O. Nebie, K. Carvalho, L. Barro, L. Delila, E. Faivre, T.Y. Renn, M.L. Chou, Y.W. Wu, A. Nyam-Erdene, S.Y. Chou, L. Buée, C.J. Hu, C.W. Peng, D. Devos, D. Blum, T. Burnouf, Human

889 platelet lysate biotherapy for traumatic brain injury: preclinical assessment, Brain 144 (2021)
890 3142-3158.
891 [21] M.L. Chou, J.W. Wu, F. Gouel, A. Jonneaux, K. Timmerman, T.Y. Renn, C. Laloux, H.M.
892 Chang, L.T. Lin, J.C. Devedjian, D. Devos, T. Burnouf, Tailor-made purified human platelet
893 lysate concentrated in neurotrophins for treatment of Parkinson's disease, Biomaterials 142
894 (2017) 77-89.
895 [22] F. Gouel, K. Timmerman, P. Gosset, C. Raoul, M. Dutheil, A. Jonneaux, G. Garçon, C.
896 Moreau, V. Danel-Brunaud, J. Duce, T. Burnouf, J.C. Devedjian, D. Devos, Whole and
897 fractionated human platelet lysate biomaterials-based biotherapy induces strong neuroprotection
898 in experimental models of amyotrophic lateral sclerosis, Biomaterials 280 (2022).
899 [23] E. Anitua, C. Pascual, R. Pérez-Gonzalez, G. Orive, E. Carro, Intranasal PRGF-Endoret
900 enhances neuronal survival and attenuates NF-κB-dependent inflammation process in a mouse
901 model of Parkinson's disease, J Control Release 203 (2015) 170-180.
902 [24] E. Anitua, C. Pascual, D. Antequera, M. Bolos, S. Padilla, G. Orive, E. Carro, Plasma rich
903 in growth factors (PRGF-Endoret) reduces neuropathologic hallmarks and improves cognitive
904 functions in an Alzheimer's disease mouse model, Neurobiol Aging 35(7) (2014) 1582-1595.
905 [25] T. Burnouf, T.L. Walker, The multifaceted role of platelets in mediating brain function,
906 Blood 140(8) (2022) 815-827.
907 [26] O. Leiter, T.L. Walker, Platelets in Neurodegenerative Conditions-Friend or Foe?, Front
908 Immunol 11 (2020) 747.
909 [27] O. Nebie, L. Buée, D. Blum, T. Burnouf, Can the administration of platelet lysates to the
910 brain help treat neurological disorders?, Cell Mol Life Sci 79(7) (2022) 379.
911 [28] J.A. Welsh, D.C. Goberdhan, L. O'Driscoll, C. Théry, K.W. Witwer, MISEV2023: An
912 updated guide to EV research and applications, Journal of Extracellular Vesicles 13(2) (2024)
913 e12416.
914 [29] D. Livkisa, T.H. Chang, T. Burnouf, A. Czosseck, N.T.N. Le, G. Shamrin, W.T. Yeh, M.
915 Kamimura, D.J. Lundy, Extracellular vesicles purified from serum-converted human platelet
916 lysates offer strong protection after cardiac ischaemia/reperfusion injury, Biomaterials 306
917 (2024) 122502.
918 [30] R. Widyaningrum, Y.W. Wu, L. Delila, D.Y. Lee, T.J. Wang, T. Burnouf, In vitro
919 evaluation of platelet extracellular vesicles (PEVs) for corneal endothelial regeneration, Platelets
920 33(8) (2022) 1237-1250.
921 [31] G.S. Liu, H.A. Chen, C.Y. Chang, Y.J. Chen, Y.Y. Wu, A. Widhibrata, Y.H. Yang, E.H.
922 Hsieh, L. Delila, I.C. Lin, T. Burnouf, C.L. Tseng, Platelet-derived extracellular vesicle drug
923 delivery system loaded with kaempferol for treating corneal neovascularization, Biomaterials
924 319 (2025) 123205.
925 [32] F. Back, A. Barras, A. Nyam-Erdene, J.C. Yang, S. Melinte, J. Rumipamba, T. Burnouf, R.
926 Boukherroub, S. Szunerits, E.Y. Chuang, Platelet Extracellular Vesicles Loaded Gelatine
927 Hydrogels for Wound Care, Adv Healthc Mater 14(1) (2025) e2401914.
928 [33] A. Nyam-Erdene, O. Nebie, L. Delila, L. Buee, D. Devos, S.Y. Chou, D. Blum, T. Burnouf,
929 Characterization and Chromatographic Isolation of Platelet Extracellular Vesicles from Human
930 Platelet Lysates for Applications in Neuroregenerative Medicine, ACS Biomater Sci Eng 7(12)
931 (2021) 5823-5835.
932 [34] M. Aatonen, S. Valkonen, A. Boing, Y. Yuana, R. Nieuwland, P. Siljander, Isolation of
933 Platelet-Derived Extracellular Vesicles, Methods Mol Biol 1545 (2017) 177-188.

[35] T.L. Walker, G. Kempermann, One mouse, two cultures: isolation and culture of adult neural stem cells from the two neurogenic zones of individual mice, J Vis Exp (84) (2014) e51225.
[36] C. Zeng, F. Pan, L.A. Jones, M.M. Lim, E.A. Griffin, Y.I. Sheline, M.A. Mintun, D.M. Holtzman, R.H. Mach, Evaluation of 5-ethynyl-2′-deoxyuridine staining as a sensitive and reliable method for studying cell proliferation in the adult nervous system, Brain Research 1319 (2010) 21-32.
[37] A. Nyam-Erdene, O. Nebie, L. Delila, L. Buée, D. Devos, S.Y. Chou, D. Blum, T. Burnouf, Characterization and Chromatographic Isolation of Platelet Extracellular Vesicles from Human Platelet Lysates for Applications in Neuroregenerative Medicine, ACS Biomater Sci Eng 7(12) (2021) 5823-5835.
[38] C.-M. Chong, N. Ai, S. Ming-Yuen Lee, ROCK in CNS: different roles of isoforms and therapeutic target for neurodegenerative disorders, Current drug targets 18(4) (2017) 455-462.
[39] E. Hollville, S.E. Romero, M. Deshmukh, Apoptotic cell death regulation in neurons, Febs j 286(17) (2019) 3276-3298.
[40] N.T.N. Le, C.L. Han, L. Delila, O. Nebie, H.T. Chien, Y.W. Wu, L. Buee, D. Blum, T. Burnouf, Proteomics of human platelet lysates and insight from animal studies on platelet protein diffusion to hippocampus upon intranasal administration, APL Bioeng 8(2) (2024) 026111.
[41] L. Delila, Y.W. Wu, O. Nebie, R. Widyaningrum, M.L. Chou, D. Devos, T. Burnouf, Extensive characterization of the composition and functional activities of five preparations of human platelet lysates for dedicated clinical uses, Platelets 32(2) (2021) 259-272.
[42] F. Gouel, B. Do Van, M.L. Chou, A. Jonneaux, C. Moreau, R. Bordet, T. Burnouf, J.C. Devedjian, D. Devos, The protective effect of human platelet lysate in models of neurodegenerative disease: involvement of the Akt and MEK pathways, J Tissue Eng Regen Med 11(11) (2017) 3236-3240.
[43] R. Crescitelli, J. Falcon-Perez, A. Hendrix, M. Lenassi, L.T.N. Minh, T. Ochiya, N. Noren Hooten, U. Sandau, C. Thery, R. Nieuwland, Reproducibility of extracellular vesicle research, J Extracell Vesicles 14(1) (2025) e70036.
[44] M. Borzello, S. Ramirez, A. Treves, I. Lee, H. Scharfman, C. Stark, J.J. Knierim, L.M. Rangel, Assessments of dentate gyrus function: discoveries and debates, Nature Reviews Neuroscience 24(8) (2023) 502-517.
[45] G. Kempermann, H. Song, F.H. Gage, Neurogenesis in the adult hippocampus, Cold Spring Harbor perspectives in biology 7(9) (2015) a018812.
[46] P. Tiwari, S. Mueed, A.O. Abdulkareem, K. Hanif, Activation of angiotensin converting enzyme 2 promotes hippocampal neurogenesis via activation of Wnt/β-catenin signaling in hypertension, Molecular and Cellular Neuroscience 130 (2024) 103953.
[47] L.N. Manganas, I. Durá, S. Osenberg, F. Semerci, M. Tosun, R. Mishra, L. Parkitny, J.M. Encinas, M. Maletic-Savatic, BASP1 labels neural stem cells in the neurogenic niches of mammalian brain, Scientific Reports 11(1) (2021) 5546.
[48] K. Ishikawa, S. Azuma, S. Ikawa, K. Semba, J.-i. Inoue, Identification of DRG family regulatory proteins (DFRPs): specific regulation of DRG1 and DRG2, Genes to cells : devoted to molecular & cellular mechanisms 10 (2005) 139-50.
[49] H. Stenmark, Rab GTPases as coordinators of vesicle traffic, Nature Reviews Molecular Cell Biology 10(8) (2009) 513-525.

[50] C. Song, W. Huang, P. Zhang, J. Shi, T. Yu, J. Wang, Y. Hu, L. Zhao, R. Zhang, G. Wang, Y. Zhang, H. Chen, H. Wang, Critical role of ROCK1 in AD pathogenesis via controlling lysosomal biogenesis and acidification, Translational Neurodegeneration 13(1) (2024) 54.
[51] S. Corbetta, S. Gualdoni, G. Ciceri, M. Monari, E. Zuccaro, V.L. Tybulewicz, I. de Curtis, Essential role of Rac1 and Rac3 GTPases in neuronal development, Faseb j 23(5) (2009) 1347-57.
[52] S. Uchida, G. Martel, A. Pavlowsky, S. Takizawa, C. Hevi, Y. Watanabe, E.R. Kandel, J.M. Alarcon, G.P. Shumyatsky, Learning-induced and stathmin-dependent changes in microtubule stability are critical for memory and disrupted in ageing, Nature Communications 5(1) (2014) 4389.
[53] L.N. Tran, S.K. Loew, S.J. Franco, Notch Signaling Plays a Dual Role in Regulating the Neuron-to-Oligodendrocyte Switch in the Developing Dorsal Forebrain, J Neurosci 43(41) (2023) 6854-6871.
[54] A. Lampada, V. Taylor, Notch signaling as a master regulator of adult neurogenesis, Frontiers in Neuroscience Volume 17 - 2023 (2023).
[55] M.J. Lazarczyk, J.E. Kemmler, B.A. Eyford, J.A. Short, M. Varghese, A. Sowa, D.R. Dickstein, F.J. Yuk, R. Puri, K.E. Biron, M. Leist, W.A. Jefferies, D.L. Dickstein, Major Histocompatibility Complex class I proteins are critical for maintaining neuronal structural complexity in the aging brain, Scientific Reports 6(1) (2016) 26199.
[56] L.M. Boulanger, MHC class I in activity-dependent structural and functional plasticity, Neuron Glia Biol 1(3) (2004) 283-9.
[57] C.J. Shatz, MHC class I: an unexpected role in neuronal plasticity, Neuron 64(1) (2009) 40-5.
[58] E. Wilson, W. Knudson, K. Newell-Litwa, Hyaluronan regulates synapse formation and function in developing neural networks, Scientific Reports 10(1) (2020) 16459.
[59] M. Schwartz, J. Kipnis, S. Rivest, A. Prat, How do immune cells support and shape the brain in health, disease, and aging?, J Neurosci 33(45) (2013) 17587-96.
[60] M. Kanmogne, R.S. Klein, Neuroprotective versus Neuroinflammatory Roles of Complement: From Development to Disease, Trends in Neurosciences 44(2) (2021) 97-109.
[61] D.P. Schafer, E.K. Lehrman, A.G. Kautzman, R. Koyama, A.R. Mardinly, R. Yamasaki, R.M. Ransohoff, M.E. Greenberg, B.A. Barres, B. Stevens, Microglia sculpt postnatal neural circuits in an activity and complement-dependent manner, Neuron 74(4) (2012) 691-705.
[62] A.K. McAllister, J. van de Water, Breaking Boundaries in Neural-Immune Interactions, Neuron 64(1) (2009) 9-12.
[63] A. Matejuk, A.A. Vandenbark, H. Offner, Cross-Talk of the CNS With Immune Cells and Functions in Health and Disease, Front Neurol 12 (2021) 672455.
[64] P.A. Carpentier, T.D. Palmer, Immune influence on adult neural stem cell regulation and function, Neuron 64(1) (2009) 79-92.

1019 **Legends**

1020 **Fig.1 Comprehensive characterization of platelet-derived extracellular vesicles (pEV) and**
1021 **HPPL isolated from clinical-grade platelet concentrates. (a)** Schematic workflow for isolation
1022 and preparation of pEVs and HPPL from clinical-grade platelet concentrate. (**b**) Representative
1023 cryo-electron microscopy (cryo-EM) images showing EVs from SCPL (left) and SEC-isolated
1024 EVs-SCPL (right). Arrows indicate characteristic double-membrane structure. Scale bar = 100 nm.
1025 (**c**) Size distribution profiles of pEVs determined by dynamic light scattering (DLS) across three
1026 independent batches (mean ± SD, n = 3). (**d**) Quantification of total particle yields from pEVs as
1027 measured by nanoparticle tracking analysis (NTA). (**e**) SDS-PAGE analysis of pEVs and HPPL
1028 under reducing and non-reducing conditions (20 µg protein/lane). Molecular weight markers are
1029 shown in the rightmost lane. (**f**) Protein concentration are shown by BCA (n=3) (**g**) Exo-Check
1030 antibody array demonstrating expression of canonical EV markers (CD63, Tsg101, and CD81) in
1031 pEVs. (**h**) Nano flow cytometric analysis of CD9 and CD41 expression in pEVs at optimized
1032 particle counts (2,000-12,000 particles/min), with size distribution and concentration determined
1033 through software calibration. (**i**) Venn diagram illustrating the proteomic profiles of pEVs and
1034 HPPL, showing the number of shared and unique proteins identified in each preparation. (**j**)
1035 Functional categorization of proteins exclusively detected in pEVs, expressed as percentage
1036 distribution across categories. (**k**) Top 10 significantly enriched proteins in pEVs and HPPL,
1037 ranked by expression ratio and quantified as log2 fold change (Log2FC) of pEVs versus HPPL.
1038
1039 **Fig.2 pEVs selectively regulate DG-derived neural precursor cell proliferation *ex vivo*. A.**
1040 Schematic representation of neural stem cell isolation from the dentate gyrus (DG) followed by
1041 neurosphere generation. **B**. Quantification of neurosphere number and size distribution from DG-
1042 derived cultures following treatment with platelet concentrate-derived extracellular vesicles (pEVs)
1043 or heat-treated platelet pellet lysate (HPPL). The size of 50 neurospheres was analyzed per
1044 condition. For neurosphere number, all visible neurospheres were counted in 80 wells of a 96-well
1045 plates per condition. Data are mean ± SEM from five independent experiments. ***$p < 0.001$ vs
1046 PBS using one-way ANOVA followed by Dunnett's multiple comparisons post-hoc test. Control
1047 condition is normalized to 100%, and that pEVs and HPPL values represent the relative change in
1048 neurosphere size and number compared to this baseline. **C.** Proliferation of DG-derived
1049 neurospheres treated with pEVs or HPPL in the absence of EGF and FGF-2. Data represent mean
1050 ± SEM from three independent experiments. $p < 0.05$ by one-way ANOVA with multiple
1051 comparisons.
1052
1053
1054 **Fig.3 pEVs selectively regulate DG neural precursor cell proliferation *in vivo* at day 3.**
1055 **A.** Schematic representation of the short-term (3-day) intranasal delivery protocol for pEVs or
1056 HPPL, combined with EdU (50 mg/kg) i.p administration twice daily at 6-hour intervals. **B.**
1057 Representative confocal images of EdU^+ cells in the DG following 3-day treatment with pEVs or
1058 HPPL. Green channel represents EdU-labeled cells, and blue channel shows DAPI nuclear staining.
1059 Images acquired by Stellaris confocal microscopy with (20× objectives). Scale bar: 100 µm (inset:
1060 50 µm). Quantification of total EdU^+ cells across 5 DG sections/animal along the granular layer in
1061 DG. Data are mean ± SEM (N = 18 animals per group). *$p < 0.05$ vs PBS using one-way ANOVA
1062 followed by Dunnett's multiple comparisons post-hoc test.

1063

1064 **Fig.4 Differentiation of neural precursor cells ex vivo under pEV and HPPL stimulation A.**
1065 Schematic representation of the experimental design for neurosphere differentiation studies under
1066 pEVs and HPPL conditions. **B.** Quantification of DCX, and NeuN-positive cells as a percentage
1067 of total DAPI-positive nuclei per field. Data represent mean ± SEM from (n=3) ordinary one-way
1068 ANOVA followed by Dunnett's (**$p < 0.01$) with multiple comparisons post-hoc test. **C.**
1069 Representative immunocytochemistry images showing DCX expression (red) in differentiated
1070 neurospheres under pEVs or HPPL treatment compared to untreated controls. Nuclei
1071 counterstained with DAPI (blue) Scale bars = 50µm **D.** Representative immunocytochemistry
1072 images of DG-derived differentiated neurospheres immunostained for NeuN (red) following pEV
1073 or HPPL treatment versus untreated controls. Nuclei counterstained with DAPI (blue) Scale bars
1074 = 50µm.

1075

1076 **Fig.5 pEVs promote neurogenesis in the dentate gyrus (DG) of hippocampus**. **A.** Experimental
1077 design schematic showing long-term (28-day) intranasal administration protocol for pEVs and
1078 HPPL combined with EdU (50 mg/kg) labeling regimen (twice daily at 6-hour intervals). **B.**
1079 Quantification shows total EdU^+ cells across 5 DG sections/animal along the granular layer in DG,
1080 percentage of co-expressing DCX^+/EdU^+ and $NeuN^+/EdU^+$ cells in the granular layer of DG region.
1081 Data represent mean ± SEM (N = 18 animals per group). Statistical significance determined by
1082 ordinary one-way ANOVA followed by Dunnett's (*$p < 0.05$, **$p < 0.01$ ***$p < 0.001$) *with*
1083 *multiple comparisons post-hoc test.* **C-D.** Representative images of immature/mature neurons co-
1084 expressing DCX^+/EdU^+ and $NeuN^+/EdU^+$ in the granular layer of DG following pEVs & HPPL
1085 treatment at day 28. DCX is illustrated by gray channel, EdU by green channel, and NeuN, by red
1086 channel. Scale bars: 50 µm; inset scale bar: 20 µm. White arrows indicate DCX^+/EdU^+, and
1087 $NeuN^+/EdU^+$ co-expressing cells, orange arrows indicate DCX^-/EdU^+, and $NeuN^-/EdU^+$ cells.
1088 Representative images were captured using Stellaris confocal microscopy with (63× objectives).
1089 Data indicate that pEVs significantly increase the proportion of $NeuN^+$ cells among EdU^+ cells in
1090 the DG, suggesting enhanced neuronal differentiation, while HPPL primarily promotes cell
1091 proliferation and increases the number of immature neurons in the DG.
1092

1093 **Fig.6 Proteomic profiling reveals pEVs-induced molecular changes in the dentate gyrus (DG)**
1094 **of hippocampus. A**. Experimental workflow showing DG tissue collection following 28-day of
1095 intranasal administration of pEVs or PBS as control, followed by proteomic profiling via LC-
1096 MS/MS. **B.** Venn diagram illustrating the overlap of identified proteins in DG tissue from pEVs
1097 and PBS-treated groups, highlighting both shared and treatment-specific proteins. **C.** The
1098 differentially expressed proteins (DEPs) were identified by comparing proteins commonly
1099 expressed between pEV-treated samples and PBS controls. Volcano plot analysis of these DEPs
1100 in DG tissue following pEV treatment revealed significant changes using thresholds of $p \leq 0.05$
1101 and fold change ≥ 1.2. Red and blue points on the plot indicate significantly upregulated and
1102 downregulated proteins, respectively. **D.** Gene Ontology (GO) enrichment of upregulated and
1103 downregulated DEPs categorized by biological process, molecular function, and cellular
1104 component. Neurogenesis Pathway Proteins Altered by EV Treatment: Upregulated and
1105 Downregulated Proteins with Log2FC Values, KEGG pathway analysis is shown for both subsets.
1106 **E.** Canonical pathway analysis of differentially expressed proteins (DEPs) using Ingenuity

Pathway Analysis (IPA), highlighting significantly altered signaling networks ($p < 0.05$) after DG_EV treatment compared to PBS. Pathways are color-coded by activation z-score: orange bars indicate predicted activation (positive z-score), blue bars indicate predicted inhibition (negative z-score), and white bars indicate pathways with z-score = 0. The green line represents the ratio of DEPs present in each pathway relative to the total proteins in that pathway.

Fig.7 STRING protein-protein interaction network analysis of upregulated and downregulated proteins in DG following pEVs treatment. (a) Network was generated using MCL clustering algorithm with inflation parameter of 3 to identify natural clusters based on stochastic flow. Network statistics: 61 nodes (proteins), 45 edges (interactions), average node degree of 1.48, and average local clustering coefficient of 0.423. The network shows significant enrichment in protein-protein interactions (PPI enrichment p-value: 0.000114) compared to expected interactions (24). Visualization parameters: maximum FDR ≤ 0.05, minimum signal ≥ 0.01, and minimum interaction strength ≥ 0.01. (b) Network was generated using MCL clustering algorithm with inflation parameter of 3 to identify natural clusters based on stochastic flow. Network statistics: 50 nodes (proteins), 34 edges (interactions), average node degree of 1.36, and average local clustering coefficient of 0.344. The network shows significant enrichment in protein-protein interactions (PPI enrichment p-value: 0.02) compared to expected interactions (23). Visualization parameters: maximum FDR ≤ 0.05, minimum signal ≥ 0.01, and minimum interaction strength ≥ 0.01.